UNIVERSITY OF CALIFORNIA
RIVERSIDE

# Computational Study of Cellular Budding at Different Physical Length Scales

A Dissertation submitted in partial satisfaction
of the requirements for the degree of

Doctor of Philosophy

in

Mathematics

by

Kevin Yueh Tsai

September 2020

Dissertation Committee:

Dr. Mark Alber, Chairperson
Dr. Weitao Chen
Dr. Qixuan Wang

The Dissertation of Kevin Yueh Tsai is approved:

---

---

---

Committee Chairperson

University of California, Riverside

## Acknowledgments

I want to extend my deepest gratitude to my advisor Dr. Mark Alber for taking me on as a student and investing countless time and resources to help me grow as a student and researcher as well for advising me on my research program and developing my scientific thinking and writing skills. I also want to extend my deepest gratitude to Dr. Roya Zandi for providing invaluable feedback and guidance, which are critical to the completion of my work, and to Dr. Weitao Chen for providing me invaluable advice and helping me shape a research problem. I also would like to acknowledge Samuel Britton for his invaluable effort and assistance in C++ and GPU implementations of my work. I would like to thank members of the mathematical biology and applied math research group at UC Riverside, who have provided invaluable supports and insights throughout my time as a graduate student. In addition, I would like to thank members of the Dr. Roya Zandi's lab of the department of physics and astronomy at UC Riverside for the valuable advice ensuring that my work is physically sounding and correct. Finally I would like to thank all my colleagues, whether we enter the program at the same year or not, for creating a excellent environment promoting mutual enrichment and emotional support.

To my father, in loving memory, who always believed in my ability to succeed and be proud of my achievements. I wish I can share with you this moment.

To my family for all the support they provided unconditionally which helped me endure through many difficulties throughout this lengthy journey.

# ABSTRACT OF THE DISSERTATION

Computational Study of Cellular Budding at Different Physical Length Scales

by

Kevin Yueh Tsai

Doctor of Philosophy, Graduate Program in Mathematics
University of California, Riverside, September 2020
Dr. Mark Alber, Chairperson

Cellular budding is an important biological process utilized by cells to survive and reproduce. It is characterized by the local protrusion on a cell surface that proceeds to form a vesicle separated from the original cell. The underlying mechanisms of cellular budding vary according to different cell types but can be generally categorized into the non-growth related and growth related process. For non-growth related budding, the process is often driven by the adhesive interaction between nanoparticle, surface-bound proteins, or actin filaments and the cell membrane at the nanometer scale. For growth related budding, similar contributors in the non-growth related budding may be present but the budding process at this scale requires recruitment of new cell surface materials. Novel tunable and biologically relevant 3D mathematical model is developed for studying the budding of yeast (Saccharomyces cerevisiae). The model incorporates growth of the cell via expansion of the cell surface and it is used to investigate the role of changes in mechanical properties on bud emergence and bud shape maintenance. Model simulations suggest that changes in the mechanical properties of the cell surface are necessary for yeast budding, and the

resulting quality of the shape of the bud depends on the types and patterns of changes. The 3D model is also applied, with modifications, to study the process of endocytosis and virus budding in the context of nanoparticle-membrane interactions. This model is capable of representing the fluidic property of the cell membrane that allows reorganization of membrane components leading to various geometrical shapes. Model computational simulations have demonstrated the impact of different levels of membrane fluidity on the efficiency and surface coverage in the wrapping of a nanoparticle by the membrane. In particular, higher level of membrane fluidity was shown to lead to efficient wrapping of the nanoparticle.

# Contents

**List of Figures** **x**

**List of Tables** **xiv**

**1 Role of combined cell membrane and wall mechanical properties regulated by polarity signals in cell budding** **1**
1.1 Introduction . . . 1
1.2 2 Methods . . . 8
1.2.1 General model description . . . 8
1.2.2 Equations of motion . . . 10
1.2.3 Interaction potentials . . . 12
1.2.4 Modeling cell growth . . . 14
1.2.5 Model calibration . . . 16
1.2.6 Numerical model implementation . . . 18
1.3 Results . . . 19
1.3.1 Role of elasticity of cell surface in yeast budding . . . 21
1.3.2 Role of the budding neck in bud formation . . . 27
1.3.3 Bud formation under different polarization patterns . . . 30
1.3.4 Bud formation under dynamic change in mechanical properties . . . 34
1.4 Discussion and conclusions . . . 40
1.4.1 Future directions . . . 46
1.4.2 Mesh refinement study . . . 47

**2 Cellular Budding at Nanometer Scale: Nanoparticle Wrapping, Endocytosis and Viral Budding** **51**
2.1 Introduction . . . 51
2.1.1 Biological background . . . 51
2.2 Modeling and method . . . 54
2.2.1 Modeling background . . . 54
2.2.2 Model description . . . 56
2.2.3 Membrane-particle interaction . . . 58
2.2.4 Membrane fluidity (viscoelasticity) . . . 59

2.2.5 Simulation method . . . . . 62
2.3 Model validation . . . . . 64
2.3.1 Viscoelastic properties . . . . . 64
2.3.2 Monte Carlo energy minimization . . . . . 65
2.4 Cell budding and endocytosis . . . . . 70
2.4.1 Comparison with existing models and theoretical predictions . . . . 70
2.4.2 Influence of membrane fluidity on budding and endocytosis . . . . . 71
2.4.3 Impact of membrane fluidity on particle wrapping efficiency . . . . . 74
2.4.4 Limitations of the current model . . . . . 79
2.4.5 Future model development . . . . . 79
2.5 Incorporating cell growth . . . . . 81
2.6 Appendix . . . . . 83

**Bibliography** **84**

# List of Figures

1.1 Experimental image (A) and representative diagram (B) of the yeast mother cell (right) and the developing bud (left) separated by the chitin and septin ring. (B) Cell wall (outer boundary) and membrane (inner boundary) are represented by two curves. Internal components of the mother cell include nucleus and vacuole. Actin cables (dashed red lines) polarize at the bud site and recruit new cell membrane/wall materials (black points). (Image A is reproduced with permission from Hanschke et al. [47]). . . . . 2

1.2 Schematic diagram of components comprising the 3D computational yeast cell model. (A) Initial simulated mother cell representation including predetermined bud region (dark grey), combined chitin and septin rings (grey tubes), and mother cell surface (light grey). (B-C) Individual model spring elements are shown at equilibrium (left) and non-equilibrium (right). . . . . 9

1.3 The growth (expansion) algorithm. Initial pair of triangles with a common edge (left) expands under stress (middle) resulting in a triangulation (right) after addition of a new node and new edges. This algorithm is used if the average area of $T_1$ and $T_2$ exceeds the critical value of $\gamma$. . . . . 15

1.4 Calibration of the mechanical model for a single yeast cell without budding. (A) Forces of opposite directions are applied to detect the elasticity properties of the cell based on a chosen parameter set. (B) The stress-strain ratio (dashed line) using parameters $k_s = 2.0$, $k_a = 2.0$ and $k_b = 0.5$. . . . . 16

1.5 Sample simulation of bud formation under uniformly altered mechanical properties of the cell surface in the budding region after different numbers of growth cycle. After protrusion occurs, the growth of the bud starts as a tubule growth (left) then transitions to a more spherical expansion (right). The strong constraint from the chitin and septin ring we impose naturally restricts the cell surface expansion at the bud neck. Between growth cycles, the system is allowed to relax and have edge connections between nodes changed. The relaxation (iterative) step size is $\Delta t = 0.001$. . . . . 20

1.6 Diagrams describing the influence of $\bar{\gamma}$ on bud emergence. (A) Variation of bending stiffness ($\alpha_b$) with fixed $\alpha_s$ and $\alpha_a$. (B) Variation of stretching stiffness ($\alpha_s$) with fixed $\alpha_b$ and $\alpha_a$. Both plots show that budding can occur when increasing $FvK$ number (dimensionless stretch-bend ratio) over a certain cutoff value, i.e. reducing $\alpha_b$ or increasing $\alpha_s$. . . . . 24
1.7 (A) Boxplot of the bud radii, $\Omega(\alpha_b, 0.05)$, for different $\alpha_b$. As $\alpha_b$ increases, the budding region becomes more resistant to bending deformation and maintains better roundness in shape, hence leading to smaller standard deviation of $\Omega(\alpha_b, 0.05)$. (B) A sample sequence of simulation snapshots for increasing values of $\alpha_b$. . . . . 26
1.8 Trend of standard deviation of selected $\Omega(\alpha_b, \bar{\gamma})$. The x-axis in each plot represents the ratio of current cell volume to the target cell volume, $1.5V_0$. The standard deviation for buds with the volume close to the target value is increased more when both $\alpha_b$ and $\bar{\gamma}$ are small. . . . . 28
1.9 (A) The approximated diameter of the bud neck plotted against stiffness of the ring $k_s^{ring} = 0, 0.25, 0.5, 1, 2.5, 10, 25, 50$. A sharp decay is observed when $k_s^{ring}$ is small. (B - D) Comparison of the bud shape and budding neck with $(\alpha_s, \alpha_b, \alpha_a) = (0.5, 0.06, 0.1)$ fixed and different rigidities of the chitin and septin ring. (B) $k_s^{ring} = 0.0$, (C) $k_s^{ring} = 0.25$, (D) $k_s^{ring} = 1.0$. The corresponding approximated standard deviations are $0.1135, 0.0980, 0.1113$ respectively, which are close to the standard deviation 0.0930 with $k_s^{ring} = 50.0$. 29
1.10 Comparison of the bud shape and budding neck under nonuniform, spatial-dependent changes in mechanical properties with different rigidities of the chitin and septin ring. The Hill coefficient is 17 and (A) $k_s^{ring} = 0.0$, (B) $k_s^{ring} = 1.0$, (C) $k_s^{ring} = 50.0$. In all three cases, the budding is initiated near the center of the budding region away from the chitin and septin ring location. However, simulations with weaker bud neck constraint lead to wider budding necks. . . . . 34
1.11 (A) Hill functions with different Hill coefficients used for spatially dependent changes in mechanical properties at the bud site. The Hill coefficients are chosen to be $n = 8, 17, 35, 70$. The weight represents level of the change, with being altered most at distance 0.0 and unaltered at distance 1.0. (B-D) Sample budding shapes based on different Hill coefficients. (B) $n = 70$, (C1, C2) $n = 35$, (D) $n = 17$. Two different shapes of the budding neck are observed for $n = 35$: non-axisymmetric bud neck (C1) and axisymmetric bud neck (C2). Between these two modes, the non-axisymmetric bud neck appears more frequently in simulations. . . . . 35

1.12 (A) Sample simulation of bud formation under temporal restoration of the cell surface mechanical properties in the budding region. After protrusion occurs, the growth of the bud starts as a tubule growth (left) then transitions to a more spherical expansion (right) compared to the simulation with time-independent changes in mechanical properties. In this example, $V_m = 2V_0$. (B) Standard deviation of bud radii vs. volume ratio $V/V_0$ . The initially high standard deviation (SD) corresponds to the tubule growth at the earliest stage of budding. The SD gradually decreases as the bud attains a more spherical shape. Higher target volume, $V_m$, implies slower restoration speed. The difference in restoration speed also affects how fast the bud growth transitions from apical (tubule) growth to isotropic growth, which later transitions into asymmetric growth as observed in the time-independent change in mechanical properties cases (i.e. fixed mechanical properties for budding region). . . . . 39
1.13 Comparison between bud shapes obtained using static mechanical properties (Section 1.3.1) and using temporal restorative mechanical properties (Section 3.4). Parameter sets used are as follows: (A) $(\alpha_s, \alpha_b, \alpha_a, \bar{\gamma}) = (0.5, 0.09, 0.1, 0.1)$, (B) $(\alpha_s, \alpha_b, \alpha_a, \bar{\gamma}) = (0.5, 0.052, 0.1, 0.05)$, (C) $(\alpha_s, \alpha_b, \alpha_a, \bar{\gamma}) = (0.5, 0.121, 0.1, 0.01)$, (D) Restorative mechanical properties with initial $(\alpha_s, \alpha_b, \alpha_a, \bar{\gamma}) = (0.5, 0.0151, 0.1, 0.05)$. The visual comparison is made at cell volume $V \approx 1.39 - 1.45V_0$. . . . . 40
1.14 (A) Sample simulation snapshot where the budding region is given the identical mechanical properties as the mother cell. The bud emergence is only possible when the new cell surface materials are introduced constantly by randomly selecting pairs of adjacent triangles in the budding region for growth. The resulting shape resembles the yeast mating process instead of yeast budding. (B) Sample simulation snapshot where $\alpha_* \geq 1$ (see section 3). Bud emergence is possible when $FvK > 2$, but the resulting bud shape and bud neck are unbiological. . . . . 42
1.15 Bud emergence diagram for simulations on the refined mesh. Refined mesh initially has 5120 triangles while the coarser mesh used in the main text has an initial mesh of 1280 triangles. Each data point represents a single trial. The results are similar to the results obtained on the coarse mesh. . . . . 48
1.16 plot of the bud neck width simulated on the refined mesh. A sharp decay is observed when $k_s^{ring} < 5$. . . . . 49
1.17 Sample snapshots of the bud formation simulations on the refined mesh. . 50

2.1 Influence of membrane fluidity in response to in-plane flow. (A) The steady-state of the solid-like system under flow. (B) Initial configuration of the fluidic system. (C) Snapshot of the fluidic system under in-plane flow. Note the change in topology allows the system to make adjustments. (D) The Poiseuille flow profile after extended simulation time. The configuration of the system shows the parabolic shape indicating the maximum velocity occurring along the central line in the x-direction. . . . . 65

2.2 Energy minimization of a polyhedron composed of 60 triangles. (A) Initial configuration. (B) The red dots indicate the positions of each pentagon. (C) Evolution of the total energy of the system under simulated annealing method. 68
2.3 Energy minimization of a polyhedron composed of 80 triangles. (A) Initial configuration. (B) Global minimal energy configuration. The red dots indicate the positions of each pentagon. (C) Evolution of the total energy of the system under simulated annealing method. Notice that the number of sampling needed is higher than the case with 60 triangles in Figure 2.2 due to the increased complexity of the configuration. . . . . 69
2.4 Comparison between simulation result of our model and existing theoretical predictions. (A) Prediction of the nanoparticle wrapping by different values of adhesive strength and range of interaction [94]. (B) The simulated result of our model for a chosen set of parameters including the membrane stiffness and adhesive interaction range. The sigmoidal curve matches qualitatively to the theoretical prediction. . . . . 71
2.5 The budding neck profile based on different adhesive strengths. The cross-sectional views are the configuration shortly before complete wrapping happens. As the adhesive strength increases, the length of the budding neck shortens. . . . . 72
2.6 Influence of fluidity on the degree of wrapping. As the fluidity increases, the simulation result approaches complete wrapping state. There is a range of $\omega$ values that produces partially wrapped nanoparticle as a steady state. . . . 75
2.7 Phase diagram of the final wrapping state for different levels of membrane fluidity depending on system temperature. Red indicates unbounded or wrapping state with less than 50% surface coverage. Pink indicates the partially wrapped state with wrapping level ranging from 50% to 90%. Light green indicates fluctuation between the partially wrapped state and the completely wrapped state. Dark green indicates the completely wrapped state. The remaining white region is the untested parameter combinations. Here $\omega$ is in the unit of $k_BT$, and note that the value of $\omega$ is purely theoretical and is not corresponding to real temperature. . . . . 76
2.8 Surface coverage of the particle interacting with a cell membrane. The fluidity of the membrane is based on a sampling size of 0.1% of the number of non-boundary edges in the model membrane. . . . . 77
2.9 Surface coverage of the particle interacting with a cell membrane. The fluidity of the membrane is based on a sampling size of 1% of the number of non-boundary edges in the model membrane. Compared to membrane with lower fluidity, the wrapping process is overall more efficient such that it takes significantly less time to achieve 70% coverage for cases with adhesion strength of 80 and 160 (Figure 2.8). . . . . 78
2.10 The diagram showing simulation process in both molecular dynamics and simulated annealing of virus budding and endocytosis. The red box indicates the steps that can be omitted if the simulation is molecular dynamics based. 83

# List of Tables


1.1 Parameters used in the model . . . . . 17
1.2 Bud emergence for different $FvK$ numbers . . . . . 22
1.3 Weights and critical values of expansion strain used . . . . . 23
1.4 Average standard deviation with different $\alpha_b$ and $\bar{\gamma}$ . . . . . 25
1.5 Optimal standard deviation (SD) of the bud for uniformly altered and restorative mechanical properties. The SDs here are the lowest value obtainable from simulations. For rows with $\alpha_b$, the values are extracted from data used earlier in this chapter. Overall, the local standard deviation of the bud using restorative mechanical properties is lower compared to the uniformly altered mechanical properties cases. . . . . 37
1.6 Comparison of the standard deviations (SD) of bud radii between cases of temporal restoration of bud mechanical properties and cases of fixed bud mechanical properties, with $\bar{\gamma} = 0.05$, on the refined mesh. . . . . 49

# Chapter 1

# Role of combined cell membrane and wall mechanical properties regulated by polarity signals in cell budding

## 1.1 Introduction

The content of this chapter is based on my recently published paper, "Role of combined cell membrane and wall mechanical properties regulated by polarity signals in cell budding," on journal of Physical Biology on August 24, 2020 [109].

In this chapter, a three-dimensional model is introduced for studying asymmetric cell growth, a prominent reproductive process utilized in many organisms to generate

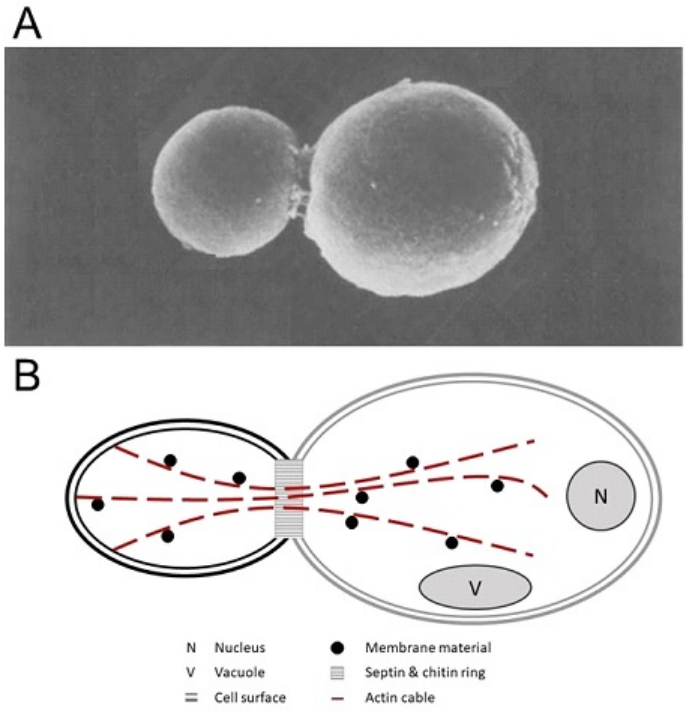


Figure 1.1: Experimental image (A) and representative diagram (B) of the yeast mother cell (right) and the developing bud (left) separated by the chitin and septin ring. (B) Cell wall (outer boundary) and membrane (inner boundary) are represented by two curves. Internal components of the mother cell include nucleus and vacuole. Actin cables (dashed red lines) polarize at the bud site and recruit new cell membrane/wall materials (black points). (Image A is reproduced with permission from Hanschke et al. [47]).

cell diversity during development. It is also important in determining cell fate when, for example, stem cells divide for the purpose of proliferation or differentiation. The budding yeast Saccharomyces cerevisiae is a fungus that can reproduce via asymmetric growth and serves as a classic model to study the principles underlying this fundamental process [27, 66, 116, 48, 54, 8, 34, 68]. Reproduction in yeast, i.e. budding, is a delicate process governed by a combination of dynamically changing biochemical signaling networks, turgor

pressure, transport of subcellular organelles, and regulation of the mechanical properties of the yeast cell surface, consisting of cell wall, cell membrane and periplasm between them.

Structurally, the yeast cell wall is a dynamic network primarily composed of polysaccharides. The cell wall network is composed of 1,3-$\beta$-glucan, 1,6-$\beta$-glucan, and a relatively small amount of chitin proteins. Linkage between the 1,3-$\beta$-glucan, 1,6-$\beta$-glucan, and chitin proteins are established to maintain the structural integrity of the cell wall [61]. Beneath the cell wall structure lies the cell membrane consisting of lipids and membrane-bound proteins similar to the membrane in animals. While the cell wall mechanically supports the cell integrity in response to forces from the environment and maintains cell shape, the cell membrane acts as the barrier to the free diffusion in the cytosol, provides binding sites for molecular signaling pathways involved in the biosynthesis of cellular components, and relays the environmental conditions to the cell interior via signaling transduction pathways to regulate the osmotic balance [49].

Yeast budding starts with a protrusion in the cell surface and results in cell division to form a daughter cell separated from the mother (Figure 1.1A). A single bud is generated in one cell cycle. Notice that no nucleus is formed yet in the bud at the early stage (Figure 1.1B) [50]. The location of the protrusion site, or the bud site, is determined by asymmetric distribution of Cdc42 and growth-associated proteins established before cell shape change, which is followed by a polarization of structural components including actin cables, septin, and myosin [19, 64]. These polarization events play an important role in budding. It has been shown experimentally that multiple concurrent protrusions during the budding process occur when the Cdc42 signaling pathway is impaired [15].

Shortly before the protrusion occurs, septins and chitins within the cell membrane and cell wall are assembled to form ring-like structures [65, 12] (Figure 1.1). It has been shown that the septin ring and the chitin ring, located in the cell membrane and cell wall, respectively, have similar functionality in controlling the size of the budding neck via different mechanisms, and the synthases responsible for the assembly of these two rings are related [98]. Presence of the rings is essential. They colocalize and, along with the linkage between the chitin ring and 1,3-$\beta$-glucan, limit the expansion along the neck during budding. Moreover, these two rings, especially the septin ring, act as a diffusion barrier impacting bud morphogenesis [8, 9]. Meanwhile, actin cables polarize to direct the transport of secretory vesicles as well as new cell membrane and cell wall materials from the cytosol to the budding site. Several studies have suggested that mutants which have improper formation of the chitin and septin rings or polarized actin cables give rise to wide budding necks, which can be detrimental to the survival of the cell [35, 36, 74].

During the early stages of the budding process, the mother cell exhibits marginal change in size and the turgor pressure remains sufficiently constant in the rage of 0.1 - 1.0 MPa [23, 97, 92]. A recent study also suggests that during the entire reproduction cycle, the turgor pressure remains at approximately 0.21 MPa [38]. While the turgor pressure acts as the driving force to generate a bulge on the cell surface, the cell wall of the bud region where Cdc42 polarizes is weakened by the secreted hydrolases and cell wall remodeling is promoted by the actin-mediated delivery of secretory vesicles [64]. This leads to degradation of the $\beta$-glucan network in the cell wall and at the same time the recruitment of new materials to the cell wall and cell membrane. While Cdc42 has not yet been reported to

directly regulate the cell surface elasticity, its polarization leads to the correct polarization of the actin cables responsible for secretory vesicle and subcellular component delivery, which has been identified in [89]. On the other hand, Cdc42 has been shown to promote cell wall degradation during yeast mating by colocalization with Fus2p protein [104, 45], demonstrating its contribution on altering cell wall properties. Hence it is reasonable to assume that the cell surface mechanical properties are indirectly regulated, if not a direct regulation, and influenced by Cdc42 polarization and its downstream processes.

However, it is challenging to experimentally measure mechanical properties of the cell surface in actively growing cells. Recently, the elasticity of the cell wall was measured during the yeast budding process and it was found that stiffness of the bud was slightly higher than that of the mother cell, although the obtained value may depend on the timing of measurements and the highly curved surface [2]. This result is different from an earlier observation in which the cell wall at the budding site becomes less rigid prior to bud emergence [64, 58]. It, therefore, remains unclear whether the change in mechanical properties of the yeast cell surface is necessary for the bud emergence. Moreover, it is not known how the mechanical properties of the cell surface are regulated to form a bud with appropriate shape.

Multiple computational models have been developed to propose and test different mechanisms underlying the budding process such as the clathrin-mediated endocytosis [26, 55] and the wrapping of nanoparticles [95, 4, 94]. In Gompper et al. [40, 41, 60], a tether-and-bead model was developed to study cell surfaces with fixed sizes and fluctuating topologies, where the cell surface was discretized by triangulated mesh and a probabilistic

re-meshing algorithm was introduced to represent cell growth. This model has been extended into a particle-based framework to study the effect of molecular turnover and the material exchange between the cell membrane and cytosol on the cell shape by incorporating a mesh-refinement algorithm [85] to facilitate the stability of the model in capturing local cell surface deformation.

On the other hand, several computational models have been developed to study morphogenesis based on description of the entire inhomogeneous cell wall. For example, in the model for mating yeast, cell wall was described as an inhomogeneous viscous fluid shell and coupled with the cell wall integrity signaling pathway, which governs the wall synthesis and controls its stiffness, to study the coordination of mechanical feedback in cell wall expansion and assembly in mating yeast [5]. Similar approach has been applied to study the tip growth of the pollen tube in plants [13]. In papers [2], the interplay between the turgor pressure and the elasto-plasticity of the cell wall during yeast budding was investigated by using a single-cell growth model (SCGM). Mother cell and bud are represented as two separate spheres with identical wall elasticity but different levels of plasticity. Growth is described by the dynamics of cell radius, which is impacted by different levels of wall plasticity and fluctuating turgor pressure. Simulation results suggest that the bud must be significantly more exposed to plastic expansion compared to the mother cell in order for proper bud formation to take place.

In this chapter, a novel 3D coarse-grained particle-based model is described and used to examine the impact of changing mechanical properties of combined cell membrane and cell wall (called cell surface hereafter) on the bud formation in yeast cells. Specifically,

model simulations show how local cell surface growth and deformation in an early bud formation, controlled by experimentally observed polarized distribution of Cdc42, impacts the global deformation of the cell surface. Model parameters were calibrated to resemble the Young's modulus of the cell wall measured in experiments [22]. The model assumes that the turgor pressure remains constant throughout the early stages of the budding process which we focus on in this chapter. Additionally, the model assumes ratios of stretching to bending modulus of the bud and mother cell to be different from each other, which is based on the experimentally observed presence of wall-degrading enzymes at the bud site.

Model simulation results indicate that increased dimensionless stretching to bending stiffness ratio, Föppl-von-Kármán number, within the bud region at the early stage can influence bud emergence and the resulting bud shape. The reduction in bending stiffness, leading to a higher Föppl-von-Kármán number, is necessary to drive bud emergence, and an unweakend or stiffer budding region leads to bud inhibition in our simulation. Chitin and septin rings were shown to impact the neck shape without changing the bud sphericity, as well as reducing the high Föppl-von-Kármán number required for bud emergence. By varying the distribution of the polarized mechanical regulator, we demonstrate that reduced polarized signal distribution may lead to asymmetric bud formation. Moreover, by assuming that the mechanical properties at the bud site can recover in time to the same level as those of the mother cell, we show that buds can acquire a symmetric shape similar to those observed in experiments. The new model can be extended to study the impact of dynamical changes of molecular distributions in yeast budding, as well as viral budding and other vegetative reproduction processes performed via budding.

## 1.2 2 Methods

### 1.2.1 General model description

Yeast mother cells can be either egg-shaped, elliptical, or spherical [24]. While the size of an yeast cell varies depending on the cell types, for simplicity we assume that the mother cell initially is a sphere with a radius of 2.0 $\mu m$ [101]. The sphere, representing the cell wall and membrane, is discretized into a triangulated mesh. The triangulated surface is a simplified representation of the elastic network of the yeast cell surface. The nodes are connected by linear springs in each triangle to capture the in-plane elasticity, whereas the bending springs are applied to triangles sharing a common edge to model the out-of-plane elasticity (Figure 1.2) [67, 88, 87]. This mesh discretization allows calibration of the model elasticity using experimental data by probing the elastic response under stress (Section 2.5). We also assume that the bud site has been predetermined and Cdc42 becomes polarized to regulate the elasticity at the bud site.

The bud site is enclosed by the chitin and septin ring which is approximately 1 $\mu m$ in diameter [16]. The size of the ring remains unchanged throughout the budding process. While the mechanical role of the ring has yet to be confirmed experimentally, the lack of the change of the ring and bud neck size, indicates a constraining effect. In the model, the bud neck is represented by using a set of linear springs with a stiffness an order of magnitude higher than the one used to model the surface of the mother resulting in a rigid ring type behaviour (1.2). Furthermore, the ring acts as a demarcation separating bud site and mother cell (**Figure 2**)[16, 37]. Distinct mechanical properties are assigned to the

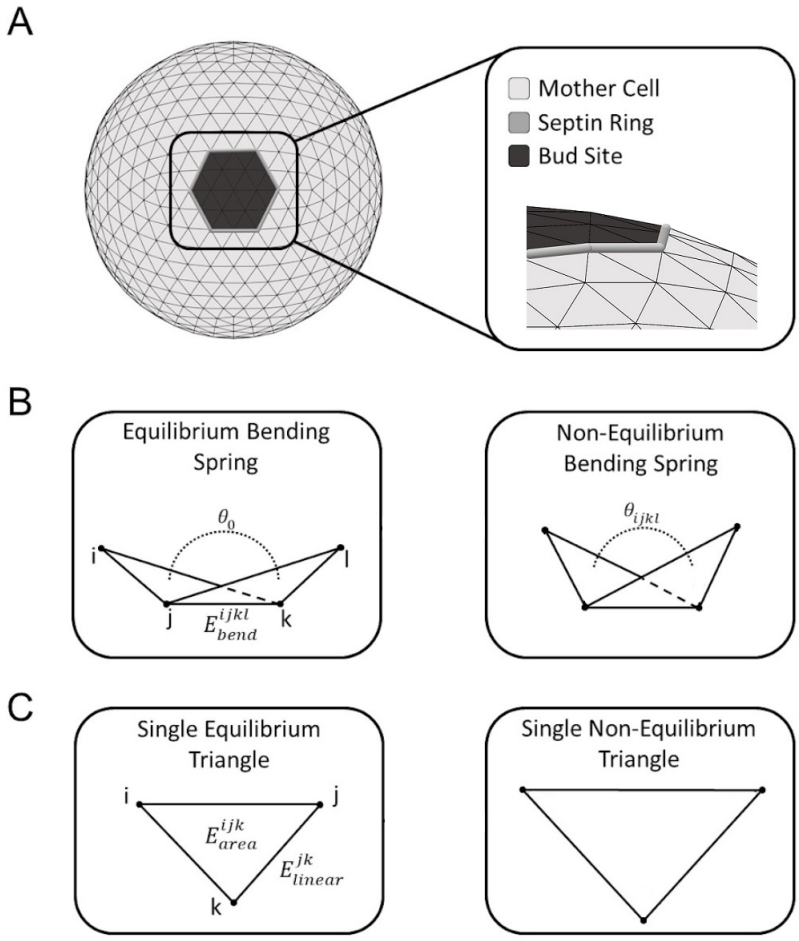


Figure 1.2: Schematic diagram of components comprising the 3D computational yeast cell model. (A) Initial simulated mother cell representation including predetermined bud region (dark grey), combined chitin and septin rings (grey tubes), and mother cell surface (light grey). (B-C) Individual model spring elements are shown at equilibrium (left) and non-equilibrium (right).

bud surface under the influence of wall degrading enzymes and to the mother cell surface. Previously developed re-meshing techniques [40, 41, 85, 1, 88] are utilized in the model to capture the structural response to osmotic pressure [69, 53].

**Computational implementation.** The iFEM [17], a MATLAB software package, was used to generate the initial mesh configuration. The density of the triangulated mesh can be changed according to the requirement of the resolution of the modeling system. In all simulations included in this chapter without specification, the number of triangles used for the mother cell at the beginning of the simulation is 1280, and out of them 24 triangles belong to the budding region. For detailed description of the numerical simulation process, see Section 2.6. The code was originally prototyped using MATLAB but was converted to C++ with GPU computing platform for improved performance[1].

### 1.2.2 Equations of motion

Motion of each node $i$ from the model representation of the cell surface is described by the following equation:

$$c\dot{x_t}(t) = -\nabla_{x_i}(E_{total}) + F_{turgor,x_i} \tag{1.1}$$

where $c$ is the friction coefficient depicting the viscosity of the cell surface, $\nabla_{x_i}$ represents the gradient with respect to the $i^{th}$ node position, $E_{total}$ represents the total potential energy used to model the mechanical properties of the surface of the cell and $F_{turgor}$ is the force derived from the force-stress relationship originating from the constant turgor pressure acting on the cell surface. The numerical integration for solving this differential equation

[1]The code is available at `https://github.com/librastar1985/Yeast_Budding`.

is performed using the standard Euler's method. (More details are provided in Sections 2.3 – 2.6.)

We define the total potential energies used to model the cell surface: $E_{total} = E_{linear} + E_{area} + E_{bend} + E_{volex}$. Here, $E_{linear}$ is the linear potential between connected nodes and $E_{volex}$ is volume exclusion property imposed between nodes that are not connected by an edge, modeling the self-avoiding property preventing cell-cell intersection. $E_{area}$ and $E_{bend}$ represent area and bending potentials yielding forces that control the area expansion resistance of each individual triangular element and level of bending between triangular elements. Due to the micron scale of the yeast cell and fluid environment required for yeast reproduction, the surrounding microenvironment acts as an overdamping media. We therefore assume that the cell in the model is in the overdamped regime where the inertia force is negligible [85, 29]. Between two successive re-meshing steps, we simulate $N_{relaxation} = 200$ iterative steps. $N_{relaxation}$ is chosen such that the relative change in total energy of the system converges to a value below a threshold of 0.01.

Notice that each mechanical potential comprising $E_{total}$ is chosen to represent cell surface elasticity, shape maintenance, and surface incompressibility, as described in Section 2.2. While the choice of the components of energy potential function is not unique, we believe that our results is inline with other form of energy potential function which have previously been used to describe the cell surface [85, 82, 83, 30]. Potentials in the model were calibrated via simulated cell stretching tests, and adjusted to match the experimental atomic force microscopy (AFM) data, as described in Section 2.2.5.

### 1.2.3 Interaction potentials

We assume linear stiffness of the cell surface under low stress and use the internodal potential for nodes connected via an edge in the following form:

$$E_{linear} = \sum_{i,j \in B(cell} \Big(\frac{k_s}{2}\Big)(L_{ij} - L_0)^2 \tag{1.2}$$

where $k_s$ is the linear spring coefficient, $L_{ij}$ is the length of the spring connecting node $i$ and node $j$, and $L_0$ is the equilibrium length of the bond. The sum is taken over all edges of the mesh, denoted by $B(cell)$. As described in Section 2.1, interactions between nodes of edges separating the budding region and the remainder of the mother cell are also represented by a similar internodal potential but the coefficient is scaled with L02. Namely, the sum of the energy potentials of the form $E^{ring}_{linear} = (k^{ring}_s/(2L_0^2))(L_{ij} - L_0)^2$ models the stiffness of segments of the chitin and septin ring on the mesh.

Following previous work [85, 82], the local area expansion resistance of each individual triangular facet is represented using a harmonic potential:

$$E_{area} = \sum_{T_{ijk} \in T(cell)} \Big(\frac{k_a}{2L_0 A_0}\Big)(A_{ijk} - A_0)^2 \tag{1.3}$$

where $k_a$ is the area expansion resistance coefficient, $A_{ijk}$ is the current area of the triangle $T_{ijk}$, $A_0$ is the equilibrium triangle area, and $L_0$ represents the equilibrium edge length in each triangular element. The sum is taken over all triangle elements $T(cell)$.

To maintain the spherical shape, we adopt the approach that utilizes the angle-bending potentials between neighboring triangles that share a common edge to enforce cell curvature. In particular, we apply the method proposed in [111]. The explicit relationship between the equilibrium angle and the radius of curvature is $sin(\theta_0)/2 \ = (12R_0^2/L_0^2 \ -3)^{-\frac{1}{2}}$

where $\theta_0$ is the equilibrium dihedral angle between unit normal vectors of edge-sharing triangles, $R_0$ is the radius of curvature, and $L_0$ is the equilibrium edge length of the triangle. Hence, the bending behavior is determined by the cosine bending potential based on the unit normal vectors of edge-sharing triangles:

$$E_{bend} = \sum_{b_{ij} \in B(cell)} k_b(1 - \cos(\theta_{ij} - \theta_0)) \tag{1.4}$$

where $k_b$ is the bending coefficient, $\theta_{ij}$ is the current dihedral angle between the unit normal vectors of two triangles sharing edge $b_{ij}$, and $\theta_0$ is the equilibrium dihedral angle. The sum is taken over all edges over the surface $B(cell)$.

Volume exclusion constraints, $E_{volex}$, are introduced to incorporate the self-avoiding property of different domains of the cell surface avoiding each other. Several models, whether with or without defining an absolute minimum distance between cell surface nodes, have employed compression-resistance potential [85, 83]. The self-avoiding property is also necessary to maintain the numerical stability and cell surface topology to avoid concavity. We apply the standard Morse potential to enforce the self-avoiding property for non-connected nodes:

$$E_{volex} = \sum_{i,j} D(1 - \exp(-a(L_{ij}^{rep} - L_0^{rep})))^2 \tag{1.5}$$

for $L_{ij}^{rep} \leq L_0^{rep}$, $j \notin N(i)$. Here $D$ represents the well depth of the Morse potential with width $a$. $L_{ij}^{rep}$ represents the distance between any two non-connecting nodes, $L_0^{rep}$ is the optimal distance between any two non-connecting nodes, and $N(i)$ is the collection of nodes connected to a given node $i$. Parameter values and the calibration are described in Section 2.2.5.

### 1.2.4 Modeling cell growth

During the budding process, the yeast cell undergoes a local deformation with a narrow neck formation and cell surface material insertion to the bud site. To capture both geometric change and the expansion of the surface, we incorporate a re-meshing technique into the model.

To alter the edge-connectivity in the current mesh, which is to obtain a new geometry favoring bud formation, we employ the Monte Carlo edge re-connectivity algorithm. The Monte Carlo simulation for edge re-connectivity (also termed bond-flip) is a well-established approach and has been shown to effectively capture the topological change which is essential in surface deformation and protein folding [1, 41, 88]. The edge re-connectivity is determined probabilistically via energy-based comparison between the pre- and post-flip of edges in the existing mesh. For a detailed description of such edge re-connectivity, please see Section 2.2.4.

In order to describe an increase of the area of the bud, we define a quantity called strain associated with the area expansion

$$\gamma = \frac{A_{ijk} - A_0}{A_0} \tag{1.6}$$

where $A_0$ is the equilibrium area and $A_{ijk}$ is the current area of the triangle. During the simulation, if the value of $\gamma$ exceeds a critical value, $\bar{\gamma}$, then new triangles are introduced into the system following the approach from [85]. Physically, this corresponds to the instance when new material insertion to the cell surface from the bulk is more energetically favorable. Biologically, it represents the response of a cell to excessive mechanical stress. Specifically, if the relative change in average area of two adjacent triangles, $T_1$ and $T_2$, is larger than

$\bar{\gamma}$, a new node, $m$, is introduced at the center of the shared edge (Figure 1.3). $T_1$ and $T_2$ are subsequently divided using the newly placed node, thereby creating four new triangles, $Q_1, \cdots, Q_4$.

To utilize this form of growth algorithm, we check this growth condition over every pair of triangles sharing a common edge inside the budding region, and call this sweeping process as one growth step.

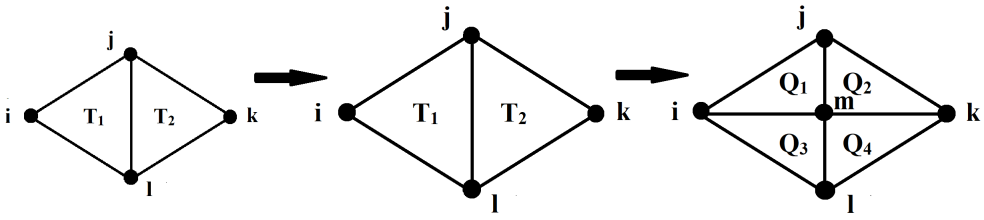


Figure 1.3: The growth (expansion) algorithm. Initial pair of triangles with a common edge (left) expands under stress (middle) resulting in a triangulation (right) after addition of a new node and new edges. This algorithm is used if the average area of $T_1$ and $T_2$ exceeds the critical value of $\gamma$.

We assume that the turgor pressure is constant at the initiation of the budding stage we model, and the surface deformation at every step is small. For each triangle in the model, the force due to the turgor pressure acting on the node $i$ is as follows,

$$F_{turgor,x_i} = \sum_{T_{ijk} \in T(i)} \frac{1}{3} A_{ijk} P \hat{n} \tag{1.7}$$

where $A_{ijk}$ is the current area of the triangle $T_{ijk}$, $P$ is the constant turgor pressure and $\hat{n}$ is the outward unit normal vector of the triangle. The sum is taken over triangles containing node $i$, denoted by $T(i)$, in order to obtain the consistent force due to the turgor pressure applied to the overall cell surface [38].

### 1.2.5 Model calibration

In experiments, whole cell compression [103] and probing via atomic force microscopy (AFM) [22] are common approaches to measure the mechanical properties of a single cell including the stretching modulus and bending modulus on the cell surface.

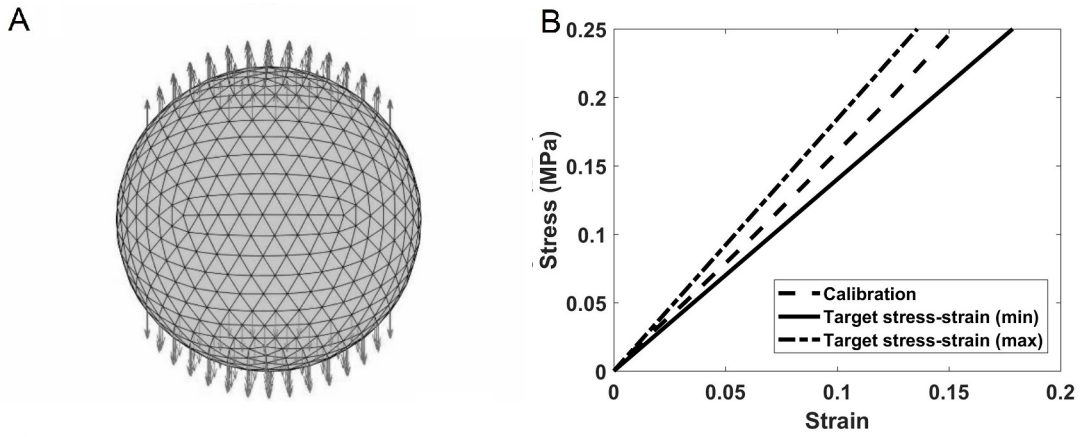


Figure 1.4: Calibration of the mechanical model for a single yeast cell without budding. (A) Forces of opposite directions are applied to detect the elasticity properties of the cell based on a chosen parameter set. (B) The stress-strain ratio (dashed line) using parameters $k_s = 2.0$, $k_a = 2.0$ and $k_b = 0.5$.

While both methods have been applied to identify the elasticity of the yeast cell wall, the reported values differ from each other by up to two orders of magnitude. The model described in this chapter was calibrated by using the measurement of the cell surface elasticity obtained by AFM in [22]. In this experiment, a nanoindentation on the cell wall was created and the modulus of elasticity was identified as $1.62 \pm 0.22$ MPa for a yeast cell prior to bud emergence.

During calibration, linear stiffness, bending stiffness and area expansion resistance coefficient are calculated after applying forces of the same magnitude in the opposite di-

rections to a single cell having initially a spherical shape (Figure 1.4A). Re-meshing is not allowed in this simulation by assuming that the cell is not actively growing at this step of the algorithm. To reduce the sample size required in exploring the parameter space, we apply Latin Hypercube Sampling to generate a sufficient amount of samples distributed over the wide range [73, 70]. Model simulations with the parameter set $k_s = 2.0,\ \ k_a = 2.0,\ k_b = 0.5$ obtained as a result of calibration, produced an elastic response which results in the correct material behavior of the cell surface, plotted in a dashed line, falling within the experimental data shown as solid lines in Figure 1.4B. We use this parameter set as the wild type condition for the mother cell in the following sections unless specified otherwise. Parameter values used in the model simulations, including the equilibrium edge length and dihedral angle, are provided in the following table.

Table 1.1: Parameters used in the model

| Parameter | Value(s) | Source |
|---|---|---|
| $k_s$ | $2.0\mu N/\mu m$ | Calibrated using AFM[22] |
| $k_b$ | $0.5\mu N\mu m$ | Calibrated using AFM[22] |
| $k_a$ | $2.0\mu N$ | Calibrated using AFM[22] |
| $k_s^{ring}$ | $50\mu N/\mu m$ | Model assumption |
| $L_0$ | $0.301\mu m$ | Relaxed initial system |
| $\theta_0$ | $0.08725rad$ | Relaxed initial system |
| $L_0^{rep}$ | $0.301\mu m$ | Model assumption |
| $D$ | 0.01 | Model assumption |
| $a$ | 9.0 | Model assumption |
| $A_0$ | $0.03927\mu m^2$ | Relaxed initial system |
| $P$ | 0.2 MPa | [38, 2] |

### 1.2.6 Numerical model implementation

Following the modeling construction described in Section 2.1, basic data structures such as the x,y,z-coordinates of each node and associated nodes for each triangle must be generated. Advanced data structures of edge-sharing triangles, connectivity between nodes, and associated edges for each triangle are necessary for inefficient simulation. These data structures are generated via both built-in functions in iFEM and in-house functions written by us. The positional update of each node is described in Section 1.2.2.

During the calibration of model parameters using the Latin Hypercube sampling (LHS), we divide the parameter value range into three uniform subspaces which in total give us 27 subspaces. We draw six sample points abiding the Latin Hypercube sampling requirements. Our initial ranges are $[0.0, 40.0]$, $[0.0, 20.0]$, and $[0.0, 40.0]$ for $k_s, k_b, k_a$, respectively. The sampling undergoes a total of six rounds of LHS, narrowing down the parameter space in each round, to reach a parameter set that grants similar elasticity from the experimental data. In each round, the subspace with the closest match to the experimental data is again divided into four subspaces. Fine tuning of the parameter set is carried out manually when the parameter set found using the sampling technique produces a fair estimate.

Numerical simulations of the model involve cycles of relaxation of the system to reach a local minimum of the total energy and growth cycles of the cell surface. During a relaxation cycle, a maximal number of $N_{relaxation} = 200$ steps, which is sufficient to approach a local minimal energy, are performed with each relaxation step size $t = 0.001$. Immediately following each relaxation cycle, the Monte Carlo based edge re-connectivity algorithm (see Section 1.2.4) is performed ([85, 1, 87]), to explore a sufficiently large number of different

edges connecting cell surface nodes prior to implementing the stochastic cell surface growth algorithm. A growth cycle is triggered after N times of edge re-connectivity algorithm implementation, where N is chosen to be 100 in our model. The numerical simulation is terminated when the total volume of the cell reaches some target value or the maximum number of steps (1.6107 steps) is reached. Note that the choices of Nrelaxation, N, and t are case dependent and adjustable in different applications to achieve both numerical stability and computational efficiency.

To accurately calculate the total cell volume, we utilize the volume formula provided in [39],

$$V = \frac{1}{6}|[\sum_{j}(P_{0j} \cdot N_j)\ |N_j \cdot \sum_{k} P_{kj} \times P_{k+1,j}|]| \tag{1.8}$$

where $P_{*j}$ are the vectors formed by connecting a reference point to each node of a given triangle in the mesh and $N_j$ is the unit normal vector of the given triangle. Using this formulation, the cell volume can be accurately calculated despite the surface concavity presented in the budding process. This formula provides the total volume using the absolute value of the sum of volumes which can be positive or negative [1]. The sign indicates whether the triangular pyramid is initiated within the interior or exterior of the surface. The total volume is calculated by summing up volumes of all the triangular pyramids created by connecting each triangle on the mesh to the center of the mother cell

## 1.3 Results

Prior to budding, Cdc42, small molecule GTPase, forms a cluster at a predetermined cortical site and orients actin cables toward the cluster. These cables then direct

delivery of more Cdc42 as well as new cell membrane and cell wall materials using secretory vesicles to the cluster. This establishes a positive feedback loop to help establish the Cdc42 polarization and regulates cell surface mechanics at the bud site to prepare for budding [64, 113, 89].

The 3D computational model described in the previous section is used to determine whether changes in the cell surface elasticity at the bud site are required for bud formation and to determine how these changes impact bud shape. In particular, we tested time-independent, spatial-dependent, and time-dependent changes in the mechanical properties, based on the spatiotemporal distribution of Cdc42 observed at different stages in experiments.

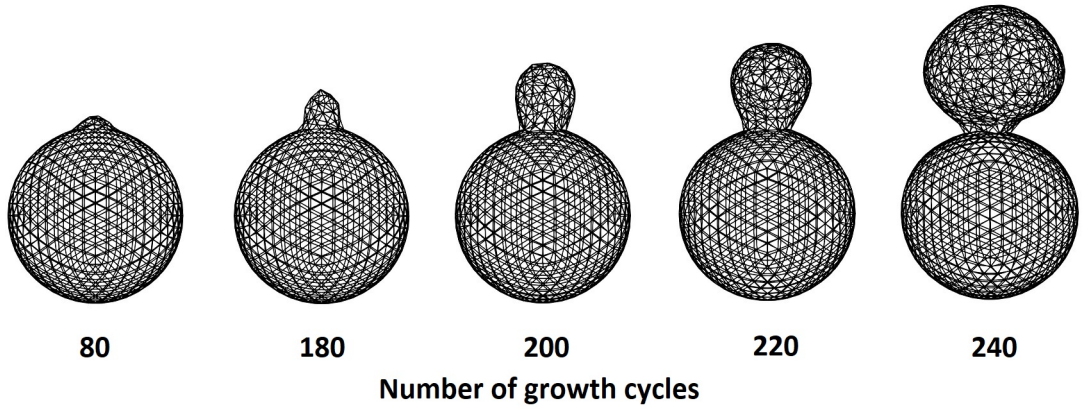


Figure 1.5: Sample simulation of bud formation under uniformly altered mechanical properties of the cell surface in the budding region after different numbers of growth cycle. After protrusion occurs, the growth of the bud starts as a tubule growth (left) then transitions to a more spherical expansion (right). The strong constraint from the chitin and septin ring we impose naturally restricts the cell surface expansion at the bud neck. Between growth cycles, the system is allowed to relax and have edge connections between nodes changed. The relaxation (iterative) step size is $\Delta t = 0.001$.

To model the impact of Cdc42 on the bud site enclosed by chitin and septin rings, each coefficient $k_*$ defined in Eq. 2-4, is multiplied by a weight constant $\alpha_*$ varied between 0.0 and 1.0 (Figure 1.2A). $\alpha_s$, $\alpha_b$, and $\alpha_a$, denote the weights for the stretching coefficient, bending coefficient, and the area expansion resistance coefficient, respectively.

In each simulation, the maximum number of iterative steps is $N = 1.6 \times 10^7$ with a total number of 800 growth steps. Since the focus of the chapter is on the early stage to mid-stage of the budding process, a simulation is terminated when all growth steps are performed or cell volume reaches 1.5 of the initial volume. All simulations described in this section used the turgor pressure $P = 0.2$ MPa. A snapshot of a typical bud emergence simulation is shown in Figure 1.5.

### 1.3.1 Role of elasticity of cell surface in yeast budding

In this section we keep the weights constant throughout the bud site in time by assuming that polarization of Cdc42 is established before the mechanical properties of the bud are changed. First, the dimensionless ratio of stretching to bending moduli and the critical value $\bar{\gamma}$ required for bud emergence are determined. Next, their impact on the shape after budding occurs is studied.

**Dimensionless ratio of stretching to bending stiffness.** In the theory of elasticity, the ratio between the stretching and bending moduli determines the physical property of the material [110, 10]. This ratio is often described by the dimensionless Föppl-von-Kármán ($FvK$) number, $k_s {L_0}^2/k_b$, where $k_s$ is the stretching stiffness, $L_0$ is an equilibrium edge length of linear spring in the mesh, and $k_b$ is the bending stiffness. By following

the same definition, we determine the range of the $FvK$ number characterizing the budding region resulting in bud generation.

**Bud emergence dependence on the Föppl-von-Kármán number.** Simulations with different $FvK$ numbers were performed to test whether a bud can be generated (Table 1). In this section, $\bar{\gamma} = 0.1$ and $\alpha_a = 0.1$ are fixed.

Table 1.2: Bud emergence for different $FvK$ numbers

| $\alpha_s$ | $\alpha_b$ | $FvK$ number | Bud Emergence |
|---|---|---|---|
| 0.2 | 0.02 | 3.624 | YES |
| 0.75 | 0.075 | 3.624 | YES |
| 0.2 | 0.05 | 1.450 | NO |
| 0.4 | 0.1 | 1.450 | NO |

The simulations suggest that bud emergence depends on the $FvK$ number. Bud emergence does not change if the $FvK$ number remains the same while weight constants $\alpha_* \leq 1$. We will discuss scenarios where $\alpha_* > 1$ in more detail toward the end of the chapter. Because the $FvK$ number is the ratio of parameters representing level of stretching and bending, for the parameter values giving the same $FvK$ number, the resulting deformations would be the same. Furthermore, this idea is used to reduce the number of parameter sets tested in our paper. Budding is more likely to occur with a sufficiently large $FvK$ number, which can be achieved by either increasing the stretching stiffness or reducing the bending stiffness.

**Bud emergence depends on critical elasticity.** We first vary bending stiffness at the bud site using weight constant $\alpha_b$, and the critical value, $\bar{\gamma}$, for Equation (1.6), to study the effect on bud formation for cell surfaces with different fixed $FvK$ numbers. Notice that according to the definition, larger $\alpha_b$ indicates stronger resistance of the cell surface

to bending deformation. Nine simulations were performed for most of the parameter sets $(\alpha_b, \bar{\gamma})$. For each simulation, the outcome was counted as a bud emergence if a visible protrusion from the cell surface with a volume at least 5.5% of the total cell volume was generated. Otherwise, it was counted as a bud inhibition and indicated by "No Bud". Different values of $\alpha_b$ and $\bar{\gamma}$ were chosen as described in Table 1.3.1. Simulation results indicate a clear cutoff value for bud emergence dependent on $(\alpha_b)$ and this cutoff reduces as increases, separating the parameter space into two different zones (Figure 1.6).

Table 1.3: Weights and critical values of expansion strain used

| | | |
|---|---|---|
| Fixed Parameter | $\alpha_s$ | 0.5 |
| Fixed Parameter | $\alpha_a$ | 0.1 |
| Variable | $\alpha_b$ | $0.052, 0.06, 0.0725, 0.09, 0.121, 0.181, 0.362$ |
| Variable | $\bar{\gamma}$ | $0.01, 0.05, 0.1, 0.15, 0.2$ |

The effect of stochasticity is insignificant for parameter sets well within these two zones. However, for simulations with parameter sets near the boundary between these two zones, the effect of stochasticity involved in the cell wall remodelling becomes more significant (Figure 1.6). In particular, with the parameters chosen near the boundary, budding can occur but not in every single trial.

Next, simulations were performed with fixed $\alpha_a$ and $\alpha_b$, and perturbed $\alpha_s$ and $\bar{\gamma}$. A cutoff value, $\alpha_s$, for bud emergence was also observed for each value of $\bar{\gamma}$ and this cutoff value increases as $\bar{\gamma}$ increases (Figure 1.6B). This is expected because bud emergence depends on the physical properties described by the $FvK$ number . The same ratio can be achieved by increasing the stretching stiffness or reducing the bending stiffness, while fixing the other.

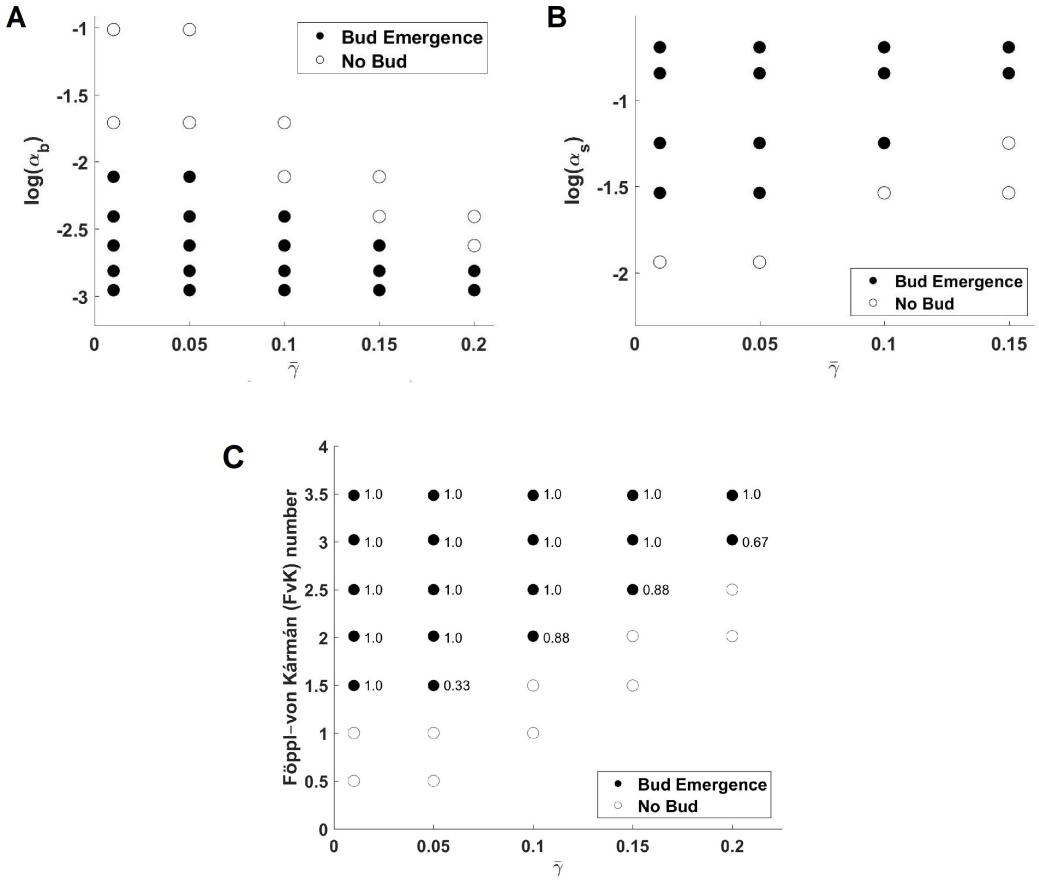


Figure 1.6: Diagrams describing the influence of $\bar{\gamma}$ on bud emergence. (A) Variation of bending stiffness ($\alpha_b$) with fixed $\alpha_s$ and $\alpha_a$. (B) Variation of stretching stiffness ($\alpha_s$) with fixed $\alpha_b$ and $\alpha_a$. Both plots show that budding can occur when increasing $FvK$ number (dimensionless stretch-bend ratio) over a certain cutoff value, i.e. reducing $\alpha_b$ or increasing $\alpha_s$.

**Impact of the Föppl-von-Kármán number on bud shape.** In this section we investigate how different ratios of stretching and bending stiffness affect the bud shape. Since increasing the stretching stiffness is equivalent to reducing the bending stiffness when changing the Föppl-von-Kármán number , in this section we fix $\alpha_s,\ \alpha_a$ and vary both $\alpha_b$ and $\bar{\gamma}$. To evaluate the sphericity of the bud, we define $\Omega(\alpha_b,\ \bar{\gamma})$ as the distances between the cell surface nodes within the bud area to the center of the bud, for given $\alpha_b$ and $\bar{\gamma}$ that can generate a bud. Here the bud center is determined by the average of the x-, y-, and z-coordinate of all nodes in the bud region. Therefore, smaller range of $\Omega(\alpha_b,\ \bar{\gamma})$ indicates more spherical shape and the average of $\Omega(\alpha_b,\ \bar{\gamma})$ represents the radius of the sphere that fits the bud. We observe that the range of $\Omega(\alpha_b,\ \bar{\gamma})$ becomes smaller as the weight $\alpha_b$ applied to the bending modulus of the bud increases for $\bar{\gamma} = 0.05$ (Figure 1.7). For different values, we observe the same trend regarding the deviation of $\Omega(\alpha_b, \bar{\gamma})$ versus $\alpha_b$ (Table 2.4). This behavior is expected as higher b leads to stronger resistance to bending deformation at the bud site and therefore more spherical shape can be maintained. We also expect more spherical shapes can be obtained when reducing the stretching modulus.

Table 1.4: Average standard deviation with different $\alpha_b$ and $\bar{\gamma}$

| | $\alpha_b = 0.052$ | 0.06 | 0.0725 | 0.09 | 0.121 |
|---|---|---|---|---|---|
| $\bar{\gamma} = 0.01$ | 0.1005 | 0.1014 | 0.1055 | 0.0746 | 0.0748 |
| $\bar{\gamma} = 0.05$ | 0.0893 | 0.0930 | 0.0743 | 0.0771 | 0.0514 |
| $\bar{\gamma} = 0.10$ | 0.0796 | 0.699 | 0.0724 | 0.0476 | No bud |
| $\bar{\gamma} = 0.15$ | 0.0586 | 0.0547 | 0.0734 | No bud | No bud |
| $\bar{\gamma} = 0.20$ | 0.0476 | 0.0644 | No bud | No bud | No bud |

This behavior is expected, as higher $\alpha_b$ leads to stronger resistance to bending deformation at the bud site and therefore more spherical shape can be maintained. We also expect more spherical shapes can be obtained when reducing the stretching modulus.

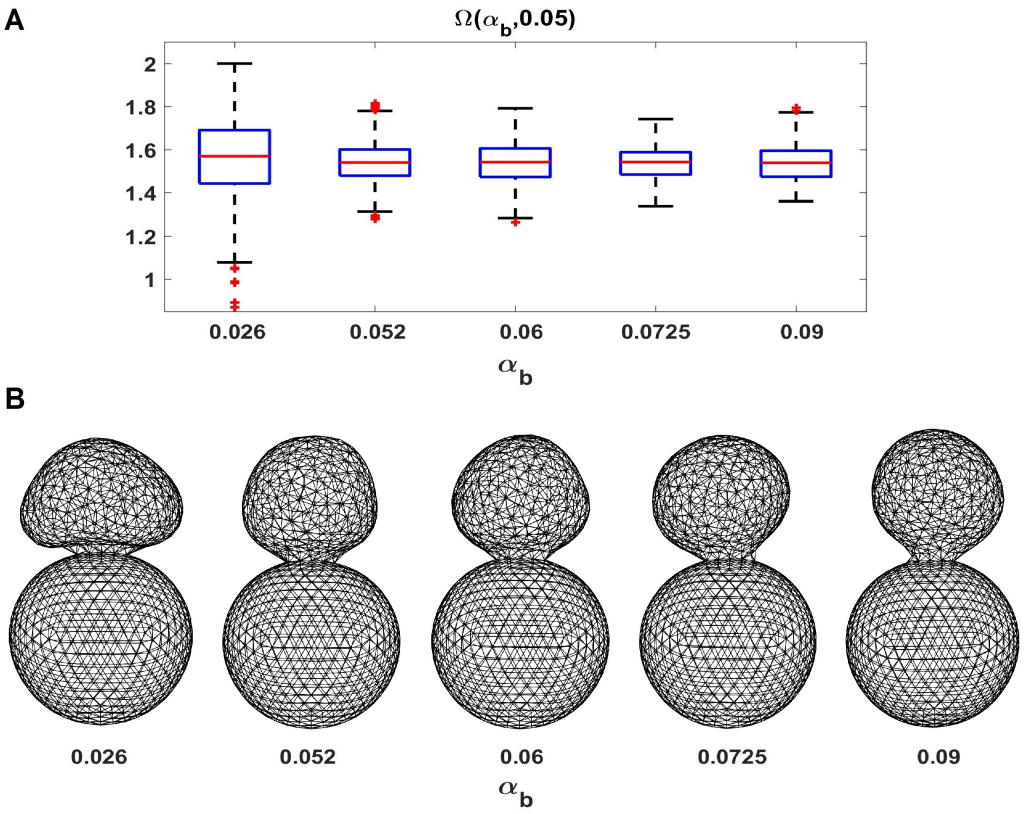


Figure 1.7: (A) Boxplot of the bud radii, $\Omega(\alpha_b, 0.05)$, for different $\alpha_b$. As $\alpha_b$ increases, the budding region becomes more resistant to bending deformation and maintains better roundness in shape, hence leading to smaller standard deviation of $\Omega(\alpha_b, 0.05)$. (B) A sample sequence of simulation snapshots for increasing values of $\alpha_b$.

Taken together, results in this section suggest a tradeoff based on $FvK$ numbers for any fixed critical value for $\gamma$, i.e. the dimensionless stretching-to-bending ratio must be sufficiently high at the bud site to generate a bud, while a higher ratio leads to less spherical bud shapes. Therefore, the ratio of stretching to bending moduli must be appropriately

tuned by the polarizing molecules to give rise to buds with spherical shapes as observed in experiments.

**Effect of the bending stiffness on the evolution of the bud shape.** The target cell volume, $1.5V_0$, is a termination criterion for simulations. We record and analyze the standard deviation of the budding process using simulations described in Section 2.3.1 that reached the target volume. Based on the simulation results, we observe an overall downward trend of the standard deviation at the early- to mid-stage of the simulation, which corresponds to the transition from apical growth to isotropic growth. Qualitatively this trend is represented by the first four snapshots of the sample simulations (Figure 1.5). Before reaching the target volume, a majority of the standard deviations increase, and cases such as $\Omega(0.052,\ 0.01)$ and $\Omega(0.0725,\ 0.01)$ show a sharp increase (Figure 1.8). However, this increase in the standard deviation can be biased due to the inclusion of the budding neck into the calculation of $\Omega(\alpha_b, \bar{\gamma})$. The increase in standard deviation can be alleviated by increasing the weight for bending stiffness or by increasing the critical value of $\gamma$. Out of all trajectories, only $\Omega(0.52,\ 0.2)$ shows consistent decrease in the standard deviation. $\Omega(0.6,\ 0.2)$, on the other hand, shows a jump in the standard deviation when the cell volume approaches the target despite higher $\alpha_b$, suggesting the behavior of $\Omega(0.52, 0.2)$ may be an isolated case.

### 1.3.2 Role of the budding neck in bud formation

It has been shown in experiments that chitin and septin ring assemblies are important in determining budding neck shape and other growth related activities during a cell

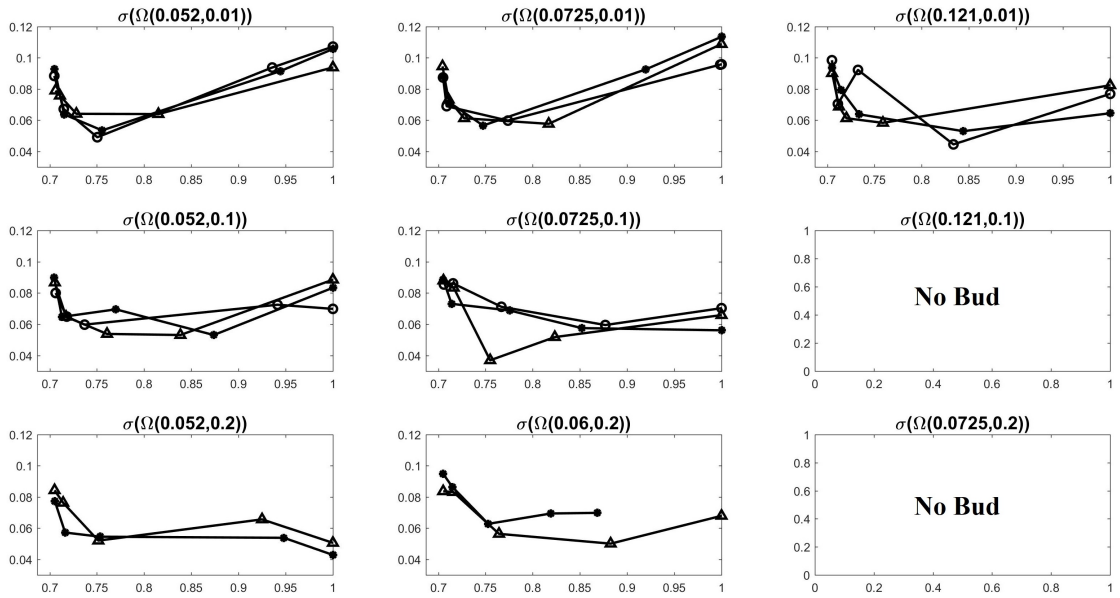


Figure 1.8: Trend of standard deviation of selected $\Omega(\alpha_b, \bar{\gamma})$. The x-axis in each plot represents the ratio of current cell volume to the target cell volume, $1.5V_0$. The standard deviation for buds with the volume close to the target value is increased more when both $\alpha_b$ and $\bar{\gamma}$ are small.

cycle [36]. In wild type yeast budding, the bud neck is roughly $1.0\mu m$ in diameter [9], while mutants with impaired chitin and septin ring can exhibit bud necks with approximately $2.68\mu m$ in diameter.

It has also been shown that the septin based ring structure acts as a diffusion barrier to the polarity factors including Cdc42 and cortical proteins, and further affects the bud shape [84]. Here we investigate the mechanical contribution of the chitin and septin rings to bud formation, as well as the shape and size of the bud neck.

Different levels of the rigidity of the combined chitin and septin ring, modeled as an elastic ring with different linear spring coefficients, ${k_s}^{ring}$, are tested and the bud neck diameter is approximated from each simulation (Figure 1.9). Consistent with experiments,

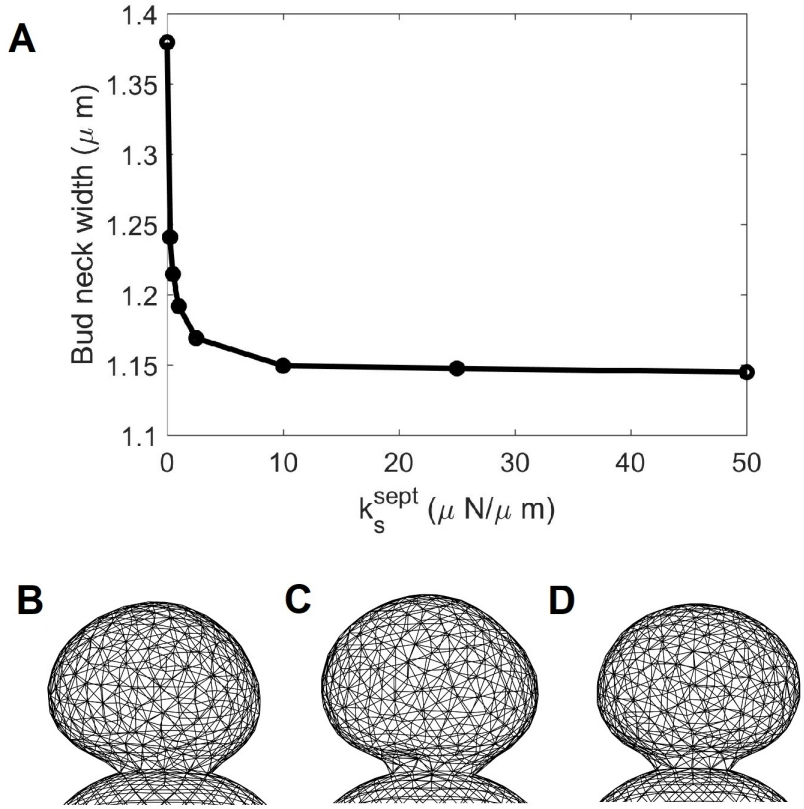


Figure 1.9: (A) The approximated diameter of the bud neck plotted against stiffness of the ring $k_s^{ring} = 0, 0.25, 0.5, 1, 2.5, 10, 25, 50$. A sharp decay is observed when $k_s^{ring}$ is small. (B - D) Comparison of the bud shape and budding neck with $(\alpha_s, \alpha_b, \alpha_a) = (0.5, 0.06, 0.1)$ fixed and different rigidities of the chitin and septin ring. (B) $k_s^{ring} = 0.0$, (C) $k_s^{ring} = 0.25$, (D) $k_s^{ring} = 1.0$. The corresponding approximated standard deviations are $0.1135, 0.0980, 0.1113$ respectively, which are close to the standard deviation 0.0930 with $k_s^{ring} = 50.0$.

a direct effect of the decreased constraint of the chitin and septin ring in the simulations is the widened budding neck. More precisely, we observe an sharp decay in the approximated budding neck diameter as ${k_s}^{ring}$ increases (Figure 1.9A).

Moreover, the standard deviation of the bud radii does not significantly depend on ${k_s}^{ring}$, ranging between 0.093 and 0.114, indicating that the rigidity of the chitin and septin ring does not impact the bud shape once budding occurs (Figure 1.9 B-D).

**Stiff chitin and septin rings slow down or prevent budding.** To demonstrate the impact of bud neck constraint originated from the chitin and septin ring on bud emergence, we choose parameter sets where bud emergence takes extraordinarily long time or is inhibited under strong bud neck constraint. For $(\alpha_s, \alpha_b, \alpha_a, \bar{\gamma}) = (0.5,\ 0.121,\ 0.1,\ 0.05)$, buds can be formed with ${k_s}^{ring} = 50.0$ and ${k_s}^{ring} = 1.0$ but the former takes about $4.12 \times 10^6$ iterative steps to reach the bud size which is half of the mother cell, while the latter takes roughly $1.06 \times 10^6$ iterative steps. Furthermore, we let $(\alpha_s, \alpha_b, \alpha_a, \bar{\gamma}) = (0.5,\ 0.181,\ 0.1,\ 0.05)$ and test the same ${k_s}^{ring}$ values, and find bud inhibition in both ${k_s}^{ring}$ values. This shows that strong bud neck constraint from the chitin and septin ring can be challenging for bud emergence if the Föppl-von-Kármán number is not sufficiently high.

To summarize, in addition to preventing the diffusion of polarity molecules involved in the budding process, the rigid chitin and septin rings impact bud emergence and determine the neck shape without changing the bud shape. The bud neck width reduces as the ring stiffness increases and high rigidity may prevent bud formation.

### 1.3.3 Bud formation under different polarization patterns

Cdc42 orients actin cables to recruit more Cdc42 as well as new cell membrane and cell wall materials before bud formation. The mechanical properties at the bud site are regulated while the polarization of Cdc42 is established. Budding can start before Cdc42 obtains sharp polarity. In this section, instead of assuming the mechanical properties are regulated by Cdc42 with a steep polarized distribution and using the constant weights

$(\alpha_s,\ \alpha_b,\ \alpha_a)$ at the bud site, we allow the mechanical properties to undergo a smooth monotonic change from the mother cell to the bud region, which are altered most at the apical tip of the bud site, and study the corresponding conditions for bud emergence and the effect on bud shape.

In particular, we apply Hill functions to model the changes in mechanical properties due to the concentrated Cdc42 along the cell membrane near the bud site, as described in the supplemental information.

We use a Hill function: $f(x) = min + (max - min)/(1 + (K/x)^n)$ where K is the midpoint between min and max, i.e. $f(K) = 0.5(min + max)$ and $x$ denotes the relative spatial position determined by the ratio $\bar{x}/X$. The numerator $\bar{x}$ is the distance between a node on the cell surface and a fixed reference point $X_0 = (x_0, y_0, z_0)$ where $x_0$ and $y_0$ are the average of the $x-$ and $y-$coordinates of all cell surface nodes, respectively, and $z_0$ is the $z-$coordinate of the tip of the bud. The denominator $X$ is calculated as $\epsilon + L_0$, where $\epsilon$ is the maximal distance between the reference point $X_0$ and the midpoint of each boundary edge of the budding region, and $L_0$ is the equilibrium edge length. The distance between the chitin/septin ring and tip of the bud is set to be the midpoint in the Hill function, K, in order to study the effect of sharpness of the changes in mechanical properties. Moreover, K is updated as the bud grows, such that the relative location of the midpoint of the weight function remains the same throughout the simulation. n is the Hill coefficient that determines the sharpness of the gradient changing from min to max, causing the function shape to be linear when $n = 1$ and change to stepwise when increasing $n$.

Because of this shape variation, we model Cdc42 distributions at different stages of polarization using a Hill function with different values of $n$. We define the weight as a spatial function of Hill type $\alpha(x) = 1/(1 + \left(\frac{x}{K}\right)^n)$ for each mechanical potential coefficient, such that $\alpha(x)$ is between 0 and 1. The Föppl-von-Kármán number is not altered when multiplied by weight 1, corresponding to the region of the mother cell, while the it is maximized when multiplied by weight 0, corresponding to the apical tip of the bud site.

To couple this Hill type weight function in the model, we start by selecting a reference point $X_0$, which is determined via the average of x- and y-coordinate of all cell surface nodes, and the z-coordinate of the tip of the budding region. The location of the chitin and septin rings relative to the average radius of the bud is always set to be the midpoint in the Hill function, $K$, in order to study the effect of sharpness of the changes in mechanical properties. Moreover, $K$ is updated as the bud grows, such that the relative location of the midpoint of the weight function remains the same throughout the simulation.

All weight functions have maximum value 1.0 in the mother cell, indicating no change in mechanical properties, and the minimum are set to be 0.5 for $\alpha_s$, 0.052 for $\alpha_b$, 0.1 for $\alpha_a$ at the bud tip, and $\bar{\gamma} = 0.05$. Different Hill coefficients $n$ are adopted to model different polarization patterns. Larger $n$ indicates a more concentrated change, i.e. the weight functions converge to the constant weights in the previous section as $n$ approaches to infinity. We test $n = 8, 17, 35, 70$ to ensure the shapes of the corresponding weight functions are distinguishable in terms of sharpness (Figure 1.11A).

We found that, for $n = 8$, the cell cannot bud. For $n = 17$, a bud successfully emerges but exhibits a much narrower hourglass-shaped neck with an approximate diameter

of $0.4 - 0.552\ \mu m$ (Figure 1.11D). For $n = 35$, two different types of budding in terms of the neck shape are observed in simulations: narrower and non-axisymmetric neck (Figure 1.11C1), and similar neck shape as the constant weight cases (Figure 1.11C2). The non-axisymmetric neck shape occurs more frequently in simulations, and the neck diameter ranges $0.87 - 1.005\ \mu m$approximately, which is calculated via the average of the max and min diameters in this case. For $n = 70$, budding can occur in a similar way as was observed when the weights were constant (Figure 1.11B), which is expected for large $n$. Moreover the resulting neck diameter was approximately $1.087 - 1.14\ \mu m$, which is similar to experimental observations.

Overall, the simulations suggest that budding emergence depends on the concentration distribution of the mechanical regulating molecules. The change in the mechanical properties at the bud site controlled by a more polarized signaling molecule is more likely to generate a bud with more robustness in the bud shape. The bud neck obtained with less polarized weight functions becomes narrower and non-axisymmetric.

**Role of chitin and septin rings by using Hill function to model the spatially dependent weights.** We perform the same model simulations with spatially dependent weight functions by altering the mechanical properties at the bud site as described in Section 1.3.1. Simulations performed with the Hill type weight functions are in agreement with the cases with constant weights. Specifically, the bud neck width reduces rapidly when ${k_s}^{ring}$ increases from 0 to 1 and remains more or less the same when ${k_s}^{ring}$ keeps increasing to 50.0.

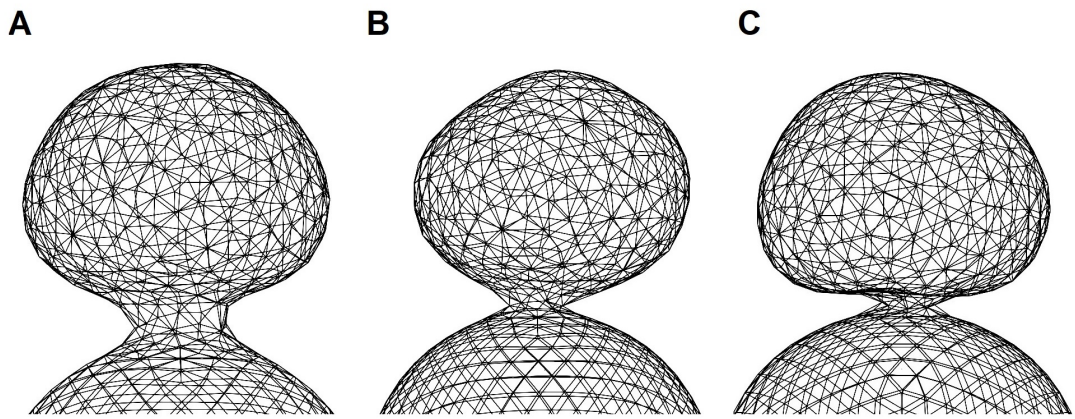


Figure 1.10: Comparison of the bud shape and budding neck under nonuniform, spatial-dependent changes in mechanical properties with different rigidities of the chitin and septin ring. The Hill coefficient is 17 and (A) $k_s^{ring} = 0.0$, (B) $k_s^{ring} = 1.0$, (C) $k_s^{ring} = 50.0$. In all three cases, the budding is initiated near the center of the budding region away from the chitin and septin ring location. However, simulations with weaker bud neck constraint lead to wider budding necks.

### 1.3.4 Bud formation under dynamic change in mechanical properties

Experiments show that Cdc42 polarizes at the apical tip region before bud formation and this highly concentrated distribution is maintained at the early stage of bud growth. As formation takes place, Cdc42 aggregates to reach a homogeneous distribution within the bud site [8]. Before cell division, Cdc42 is redirected from the bud cortex to the bud neck. This suggests that regulation of the mechanical properties might change temporally with strongest effect before bud formation or right after the apical protrusion. Therefore, we test a temporal restoration of altered mechanical properties at the bud site in our model to see whether the strong mechanical regulation, if only present in a short period at the beginning of the budding process, is sufficient or not.

**Temporal restoration functions.** Due to the energy dissipation approach used for mechanical relaxation in our simulations, the temporal restoration of the bud mechanical

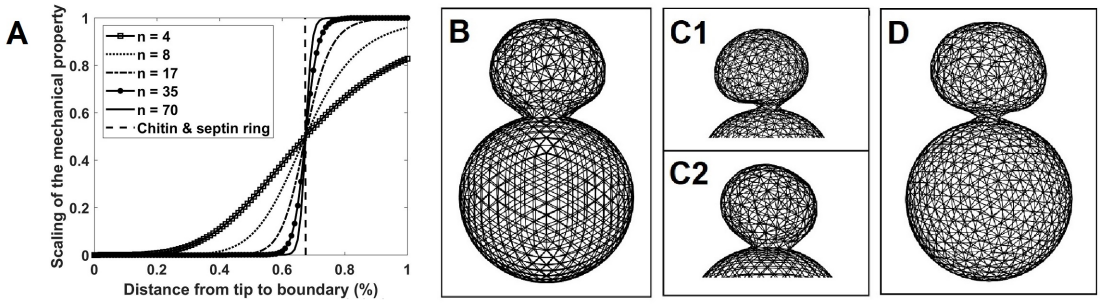


Figure 1.11: (A) Hill functions with different Hill coefficients used for spatially dependent changes in mechanical properties at the bud site. The Hill coefficients are chosen to be $n = 8, 17, 35, 70$. The weight represents level of the change, with being altered most at distance 0.0 and unaltered at distance 1.0. (B-D) Sample budding shapes based on different Hill coefficients. (B) $n = 70$, (C1, C2) $n = 35$, (D) $n = 17$. Two different shapes of the budding neck are observed for $n = 35$: non-axisymmetric bud neck (C1) and axisymmetric bud neck (C2). Between these two modes, the non-axisymmetric bud neck appears more frequently in simulations.

properties is assumed to be cell volume based, i.e., the evolution in time of the weights in altering mechanical potentials at the bud site is assumed to be linearly increasing with respect to the volume:

$$\alpha_{(i,V)}k_i = \alpha_{(i,0)}k_i + (\alpha_{(i,V')}k_i - \alpha_{(i,V_0)}k_i)(V - V_0)/(V_m - V_0) \tag{1.9}$$

$$i \in \{s, b, a\} \tag{1.10}$$

Here $\alpha_{(i,V)}$ represents the weight applied to the linear spring potential ($k_s$), cosine bending potential ($k_b$), or the area expansion resistance ($k_a$), based on the current volume $V$. When the volume reaches the target volume $V_m$, the mechanical properties of the bud become identical to those of the mother cell. Here, $V_0$ represents the initial volume of the cell.

**Temporal restoration of bud mechanical properties leads to symmetric bud shape.** To test different restoration speeds from the altered state, we change the value

of $V_m$. For example, the mechanical properties at the bud site will be fully restored to the same level as the mother cell when the cell volume doubles, i.e. $V_m = 2V_0$.

Similarly, setting $V_m = 1.5V_0$ and $V_m = 3V_0$ lead to expedited and delayed restoration compared to $V_m = 2V_0$, respectively. Based on the results of model calibration, we test the following parameter set as the altered state: $(\alpha_{s,V_0},\ \alpha_{b,V_0},\ \alpha_{a,V_0},\ \bar{\gamma}) = (0.5,\ 0.0151,\ 0.1,\ 0.05)$. In simulations, the weights $\alpha_s,\ \alpha_b,\ \alpha_a$ are changed in time following Eq.1.9 We found that temporal restoration of the mechanical properties leads to bud formation with more spherical and symmetric shapes (Figure 1.13). Regardless of different choices of the restoration speed, improved bud roundness was observed once the bud formed (Figure 1.12A). Namely, we compared the local standard deviations between buds satisfying total cell volume lies within $1.39V_0 - 1.45V_0$ . Among these simulations, we choose those with a parameter set containing $\bar{\gamma} = 0.05$ and $\alpha_s = 0.5$. Aside from the overall standard deviation (SD) calculated over the whole bud, the local standard deviation is selected to make a more detailed comparison. These SDs are quantified by using the upper hemisphere of the bud, denoted $SD_u$, lower hemisphere of the bud, denoted $SD_l$, and standard deviation of the bud excluding the budding neck, $SD_n$. $SD_u$ is calculated using cell surface nodes positioned above the center of the bud. $SD_l$ is calculated using cell surface nodes positioned between the bud neck and the center of the bud. $SD_n$ is calculated by considering only nodes whose z-coordinates are in the upper 90% of the height of the bud. The optimal values, based on $SD_n$, are presented in **Table 2.5**.

In addition, we observed that the restoration speed had a significant impact on bud formation, as faster restoration led to bud inhibition, such as $V_m = 1.5V_0$. On the other

Table 1.5: Optimal standard deviation (SD) of the bud for uniformly altered and restorative mechanical properties. The SDs here are the lowest value obtainable from simulations. For rows with $\alpha_b$, the values are extracted from data used earlier in this chapter. Overall, the local standard deviation of the bud using restorative mechanical properties is lower compared to the uniformly altered mechanical properties cases.

| | Overall SD | $SD_u$ | $SD_l$ | $SD_n$ |
|---|---|---|---|---|
| $\alpha_b = 0.052$ | 0.0630 | 0.0490 | 0.0663 | 0.0602 |
| $\alpha_b = 0.06$ | 0.0850 | 0.0766 | 0.0824 | 0.0836 |
| $\alpha_b = 0.09$ | 0.0707 | 0.0707 | 0.0630 | 0.0671 |
| $\alpha_b = 0.121$ | 0.0514 | 0.0409 | 0.0596 | 0.0425 |
| $V_m = 2.0V_0$ | 0.0415 | 0.0368 | 0.0455 | 0.0350 |
| $V_m = 3.0V_0$ | 0.0568 | 0.0544 | 0.0577 | 0.0552 |
| $V_m = 1.75V_0$ | 0.0369 | 0.0282 | 0.0438 | 0.0268 |

hand, when the restoration speed was slower, such as $V_m = 3.0V_0$, the simulation showed asymmetric growth.

As the growth of the bud always starts with a tubule, the standard deviation is higher at the early stage. Afterwards, the bud growth becomes more isotropic, and the standard deviation reduces. After that, asymmetric expansion leads to an increasing standard deviation at the late stage of the simulation. Therefore, the overall curve of the standard deviation shows nonlinearity. The speed of restoration also affects the standard deviation. More specifically, slow restoration results in fast transition from tubule growth (high standard deviation) to isotropic growth (low standard deviation). In addition, slow restoration also leads to high standard deviation during the late stage of simulation.

For $V_m = 3V_0$, the bud is initially generated in a spherical shape. Due to the slow restoration of mechanical properties allowing efficient expansion of the bud, the bud shape gradually becomes more ellipsoidal, thereby achieving a standard deviation of bud radii similar to which is observed under time-independent changes in mechanical properties. This suggests a well-coordinated restoration of the bud mechanical properties may be necessary

for symmetry maintenance of the bud. For $V_m = 2V_0$, a more symmetric bud shape is maintained after protrusion in comparison with the time-independent cases presented in Section 1.3.1 (Figure 1.13).

Here, we compare the bud shapes with the similar volumes under different patterns of changes in the mechanical properties. According to the standard deviation of bud radii, bud shape is more spherical with the temporal restoration as described in Section 1.3.1 and can be observed visually.

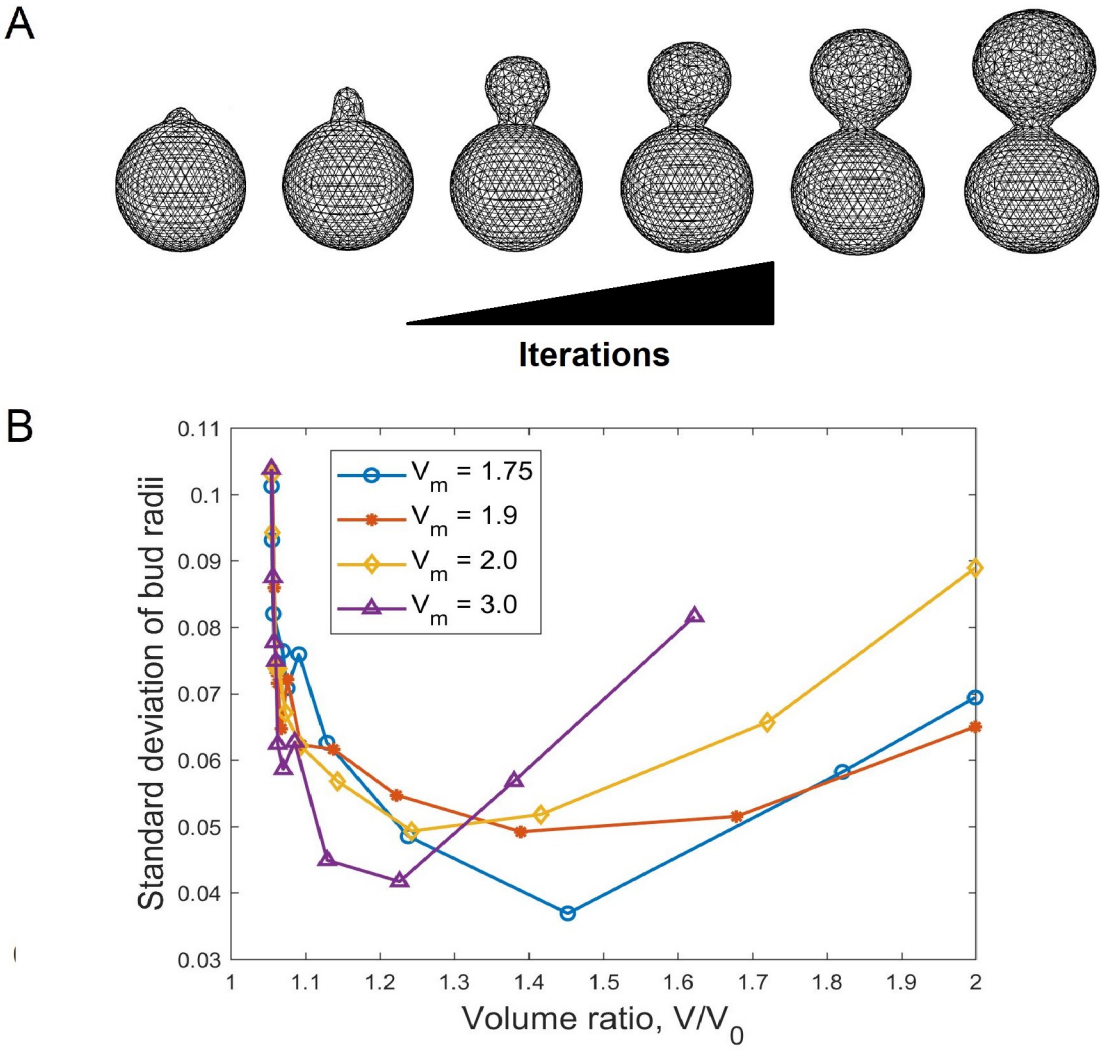


Figure 1.12: (A) Sample simulation of bud formation under temporal restoration of the cell surface mechanical properties in the budding region. After protrusion occurs, the growth of the bud starts as a tubule growth (left) then transitions to a more spherical expansion (right) compared to the simulation with time-independent changes in mechanical properties. In this example, $V_m = 2V_0$. (B) Standard deviation of bud radii vs. volume ratio $V/V_0$ . The initially high standard deviation (SD) corresponds to the tubule growth at the earliest stage of budding. The SD gradually decreases as the bud attains a more spherical shape. Higher target volume, $V_m$, implies slower restoration speed. The difference in restoration speed also affects how fast the bud growth transitions from apical (tubule) growth to isotropic growth, which later transitions into asymmetric growth as observed in the time-independent change in mechanical properties cases (i.e. fixed mechanical properties for budding region).

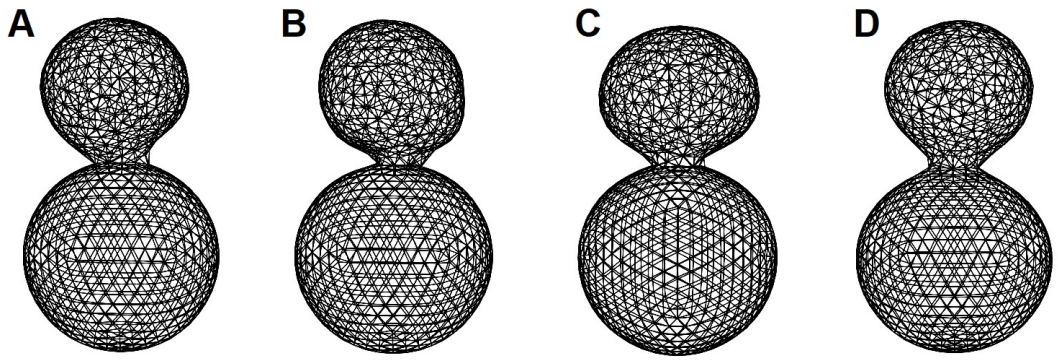


Figure 1.13: Comparison between bud shapes obtained using static mechanical properties (Section 1.3.1) and using temporal restorative mechanical properties (Section 3.4). Parameter sets used are as follows: (A) $(\alpha_s, \alpha_b, \alpha_a, \bar{\gamma}) = (0.5, 0.09, 0.1, 0.1)$, (B) $(\alpha_s, \alpha_b, \alpha_a, \bar{\gamma}) = (0.5, 0.052, 0.1, 0.05)$, (C) $(\alpha_s, \alpha_b, \alpha_a, \bar{\gamma}) = (0.5, 0.121, 0.1, 0.01)$, (D) Restorative mechanical properties with initial $(\alpha_s, \alpha_b, \alpha_a, \bar{\gamma}) = (0.5, 0.0151, 0.1, 0.05)$. The visual comparison is made at cell volume $V \approx 1.39 - 1.45V_0$.

## 1.4 Discussion and conclusions

In this chapter, a novel 3D coarse-grained particle-based model of a single cell is introduced and used to investigate the role of local changes in cell surface mechanical properties during the early stages of yeast budding. The model combines nonhomogeneous representation of the cell surface with stiff ring structures to study cell growth and budding. It is calibrated using experimentally measured Young's modulus of the budding yeast cell wall [22]. The novelty of this study lies in testing a novel hypothesized mechanism of cell budding combining changing mechanical properties of the budding region with the impact from the constraint of chitin and septin rings.

**Role of the change in mechanical properties.** Model simulations supported the hypothesis that the bud cannot emerge unless the mechanical properties are weakened in the bud region. We also demonstrated that in the case of the bud region being as rigid as,

or even more rigid than the mother cell at the early stage of budding, budding either fails to occur or occurs with a highly unbiological shape. By assuming mechanical properties being weakened uniformly at the bud site by the polarized molecules, bud emergence was shown to depend on the $FvK$ number (dimensionless ratio between stretching and bending moduli). Computationally when the velocity of adding new cell wall materials is reduced by increasing the target strain for area expansion, $\bar{\gamma}$ , bud formation requires a higher $FvK$ number when weakening the cell surface of the bud.

**Growth and maintenance of the shape of the bud.** For an emerging bud, symmetrical shape is biologically important because it indicates the balance between the composition and integrity of the bud surface, which is observed in wild type yeast budding. The sphericity of the bud shape, described via standard deviation of the bud radii, was shown to be lower for: (1) comparatively less weakened bud cell surface characterized by lower $FvK$ numbers or (2) reduced rate of cell surface material insertion characterized by the increase in critical value of $\gamma$. It is known that the chitin and septin rings serve as diffusion barriers for polarity factors at the early stage of budding. By using a computational model, we found that the resistance provided by the stiff rings prevents or slows bud growth. We also showed that neck diameter reduces as the stiffness increases, without affecting the bud shape. Also, by testing bud mechanical properties being altered by polarizing molecules with different distributions at the bud site throughout the duration of the budding process, it was shown that a cell was more likely to generate a bud with a more symmetric shape under a more polarized distribution. The bud neck obtained with less polarized distributions was narrower and non-axisymmetric.

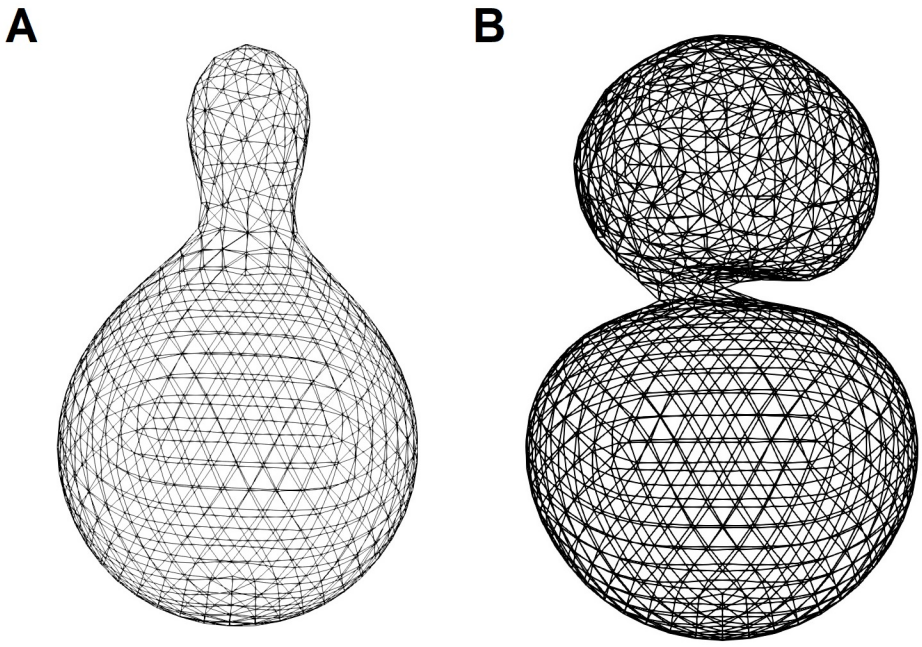


Figure 1.14: (A) Sample simulation snapshot where the budding region is given the identical mechanical properties as the mother cell. The bud emergence is only possible when the new cell surface materials are introduced constantly by randomly selecting pairs of adjacent triangles in the budding region for growth. The resulting shape resembles the yeast mating process instead of yeast budding. (B) Sample simulation snapshot where $\alpha_* \geq 1$ (see section 3). Bud emergence is possible when $FvK > 2$, but the resulting bud shape and bud neck are unbiological.

**Role of the temporal change in bud mechanical properties.** By incorporating a dynamical restoration of weakened bud mechanical properties to the level of the mother cell at the bud site, the resulting bud shape was shown to be more symmetric and spherical, as compared with the ones with fixed mechanical properties. Fast restoration was shown to prevent bud formation and slow restoration to lead to development of an asymmetric bud.

**Computational implementation of the model.** In this study, the triangular mesh was used to directly model mechanical properties of a budding yeast cell. This is different from another more traditional approach where the triangular mesh is used as the discretization technique to approximate solutions to partial differential equations. In our mechanical model, by using parameters scaled with specific mesh size in energy functions, all the mechanical properties remain the same and the simulation results under different conditions should not be affected by the mesh size [59]. To verify that simulation outcomes are independent of the mesh size, we have tested our model on a refined mesh, which initially consists of 5120 triangles, and obtained the same conclusions as those obtained on the coarser mesh. In order to achieve both accuracy and efficiency of the numerical simulations, we used a coarser mesh with 1280 triangles as the initial condition for all simulations in the paper. Detail of mesh refinement study is presented in Section 1.4.2.

**Model calibration.** So far the model was calibrated based on the mechanical properties of the mother cell, final bud neck size and bud shape. We also intend to calibrate the time scale in future using more precise and consistent experimental data such as velocities of emerging buds, when it becomes available. Notice that model simulations show

that different mechanical properties of the bud region give rise to different velocities of bud growth. We hope that our model predictions might motivate experimentalists to conduct measurements of bud mechanical properties, e.g. AFM measurements, during bud initiation. Once the time series of experimental measurements becomes available, our model can be calibrated to replace relaxation time step by biologically realistic time. An example of the calibration of the time scale under the assumption that the bud surface area increases linearly in time as follows:

In order to calibrate the time scale of the model, it is important to obtain the mechanical properties in the bud region and velocities of emerging buds in experiments, which are currently still insufficient and not consistently verified in this field [32, 59, 2]. Here we propose a method to calibrate the time scale of our model by assuming that the bud surface area linearly increases in time. It can be generalized to calibrate the model if different mechanical properties or different rates of the bud growth are obtained in experiments. In Klis et al. [59], it is suggested that surface area of the growing buds increases linearly and the rate of cell surface expansion is approximately $0.67\mu m^2/min$. Based on this data, the time required for a bud to reach 50% of the mother cell volume is approximately 44 minutes. To model the constant cell surface expansion, we modified the growth algorithm used in this paper by introducing an upper limit on the amount of cell surface material that can be introduced during each cell growth cycle. Without introducing the upper limit, the expansion rate will become unbounded in the simulation.

Let the target area threshold $\bar{\gamma} = 0.05$ and set the upper limit of the number of new nodes added per growth cycle to be one, then the cell surface expands by approximately

$0.0741\mu m^2$ during each growth cycle. Simulations showed that in order to reach a local minimum of the total energy, it was enough to use relaxation step $\Delta t = 0.001$ and perform 750 relaxation steps during each relaxation cycle. The edge re-connectivity algorithm is applied once every 50 relaxation steps to improve sphericity and smoothness of the bud surface. In calibration simulations, it took approximately 520 relaxation and growth cycles to reach the target volume of the growing bud. Since the bud surface expansion is linear, each relaxation cycle and growth cycle correspond to the same time period in experiments. Therefore, each relaxation cycle is equivalent to $44min/520 \approx 0.0846min$ and each relaxation step is equivalent to $0.0846min/750 = 1.128 \times 10^{-4}min \approx 0.00677seconds$ in real time. Therefore, the relaxation step $\Delta t = 0.001$ in the simulation corresponds to 0.00677 seconds in experiments.

Based on this calibration, we found that the growth algorithm gave rise to approximately $0.58\mu m^2/min$ expansion rate of the bug surface, which is close to the experimentally observed value. However, this time calibration is only meaningful if either the bud mechanical properties or the target area threshold are experimentally obtained. The same approach can be applied for the time scale calibration if different mechanical properties or different are measured in experiments.

**Testable predictions and suggested experiments.** Our model simulation results also predict that budding can occur only if the bud region becomes less rigid and easier to bend at the early stage, which might be due to the degradation of cell wall components. To test this prediction, experiments can be carried out to measure the mechanical properties of the bud region during the initiation of budding. The underlying mechanism

can be further investigated by applying cell wall degrading enzymes to a normal yeast cell and measuring the consequent mechanical change in the cell wall $\beta$-glucan network. Biologically a bud should eventually achieve surface elasticity comparable to the mother cell, otherwise multiple rounds of reproduction will lead to defective cells with a highly weakened cell surface. To verify that, experimental measurements of the mechanical properties of the bud region at different stages of budding are needed. Coincidentally, the polarization signal Cdc42 loses its polarized state after some time during the budding process. A time series of measurements of the surface elasticity and the Cdc42 distribution could confirm predictions of the temporal change on the bud mechanical properties obtained by our model.

### 1.4.1 Future directions

The 3D model described in this chapter, although calibrated by using data for budding yeast, can be applied to study cell growth and budding in other biological systems. It allows one to study the effect of local regulation of mechanical properties leading to global morphological changes. For instance, investigating how adverse effects due to local perturbations in the mechanical properties can propagate during growth is important for getting a better understanding of morphogenesis. In future, we plan to include in the modeling approach dynamic biochemical signaling networks submodel coupled with the cellular and subcellular mechanical submodels.

Namely, to investigate the regulation of the mechanical properties more precisely, it is worthwhile to include the model of spatiotemporal dynamics of the signaling molecules. The triangular mesh used for the mechanical model, with re-meshing techniques implemented to improve the element regularity, would be used to simulate diffusion-reaction

systems of equations describing biochemical signals. Several studies have already studied the connection between biochemical signalling and cell mechanics in mating yeast and tubule formation [5, 18, 108]. However, understanding of the coupling between the biochemical signaling pathways and cell mechanics for the yeast budding process is still incomplete. A biologically calibrated mechano-chemical model would be helpful providing predictions to be tested in future experiments.

The model described in this chapter oversimplifies contributions from cytosol components of the cell including nucleus, vacuole and actin-filaments. At the same time, the actin-filaments play a very significant role in cell surface expansion [76, 3, 114]. The nucleus also plays an important role especially in G2 and M phases of the cell cycle [52]. Recently our group developed a more refined 2D mechanical SCE type model with detailed description of the nucleus, actomyosin and cadherin, to study tissue bending mechanisms in a wing of a Drosophila embryo [79]. We are now working on incorporating these new components as well as biochemical submodel into our 3D model of an asymmetric cell growth which can be also used for studying viral budding and other vegetative reproduction processes performed via budding.

### 1.4.2 Mesh refinement study

To study the effect of mesh refinement, we refined the mesh initially used (1280 triangles) to a mesh with 5120 triangles. Bud emergence behavior is similar between the coarser and refined mesh (Figure 1.15).

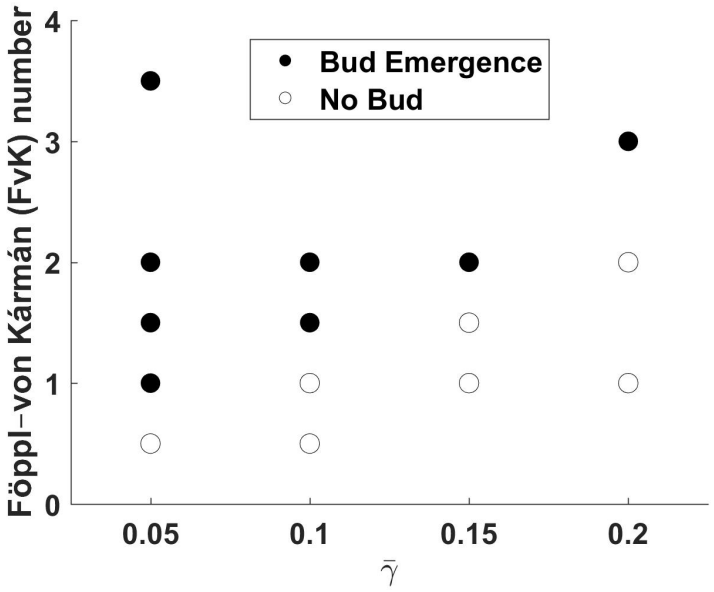


Figure 1.15: Bud emergence diagram for simulations on the refined mesh. Refined mesh initially has 5120 triangles while the coarser mesh used in the main text has an initial mesh of 1280 triangles. Each data point represents a single trial. The results are similar to the results obtained on the coarse mesh.

We showed earlier that varying the stiffness of the ring structure affects bud neck width in simulations on a coarser mesh (Figure 1.9). Simulations on a finer mesh show that bud neck width undergoes a sharp decay as the stiffness increases. Results are similar to the ones obtained on the coarser mesh. On both coarser and refined meshes, the cell surface with the highly negative curvature near the neck region was maintained once a bud formed (Figure 1.16).

Simulations on both coarse and refined meshes demonstrate that temporal restoration of bud mechanical properties leads to more symmetric bud shape. Faster restoration to the level of the mother gives rise to more symmetric budding (Table 2.6).

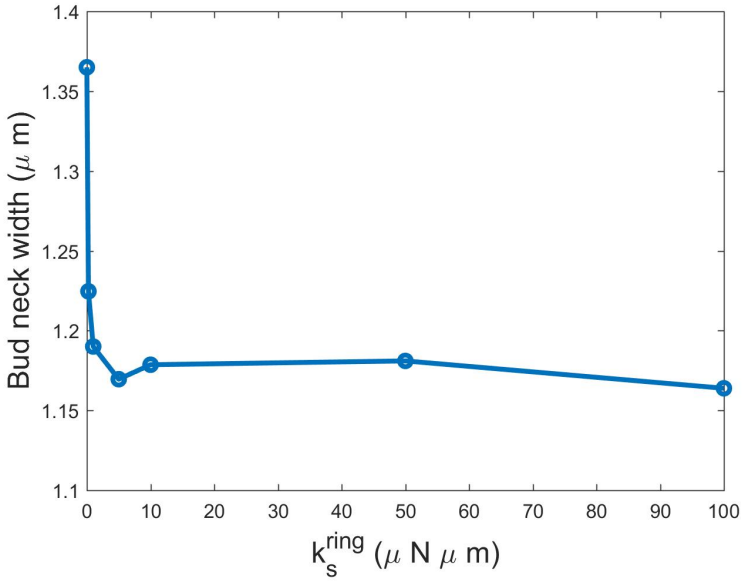


Figure 1.16: plot of the bud neck width simulated on the refined mesh. A sharp decay is observed when $k_s^{ring} < 5$.

Table 1.6: Comparison of the standard deviations (SD) of bud radii between cases of temporal restoration of bud mechanical properties and cases of fixed bud mechanical properties, with $\bar{\gamma} = 0.05$, on the refined mesh.

| $FvK$ | 1.0 | 1.5 | 2.0 | 3.5 |
|---|---|---|---|---|
| $SD$ | 0.1288 | 1.1319 | 0.2031 | 0.3262 |
| $V_m$ | 1.25 | 1.5 | 1.75 | |
| $SD$ | 0.0981 | 0.1054 | 0.1217 | |

The comparison is made at $V = 1.5V_0$. The temporal restoration cases were performed for $FvK = 3.5$ as initial condition and mechanical properties in the bud region were allowed to gradually be restored to those of the mother cell at different cell volumes $V_m$. While the values of the standard deviation obtained on the refined mesh are slightly higher than those obtained on the coarser mesh, the qualitative trend remains the same. The discrepancy in the values obtained in cases of different mesh sizes may be due to the sample size and the stochastic components of the model. Sample snapshots of the bud

formation on the refined mesh are provided in Figure 1.17. Shape evolution is similar to those obtained on the coarser mesh.

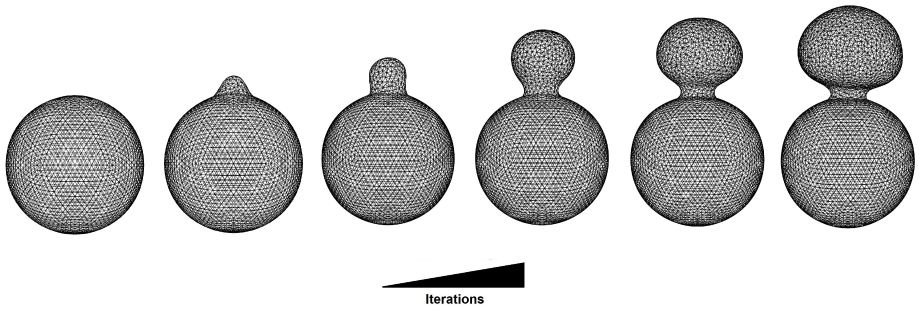


Figure 1.17: Sample snapshots of the bud formation simulations on the refined mesh.

# Chapter 2

# Cellular Budding at Nanometer Scale: Nanoparticle Wrapping, Endocytosis and Viral Budding

## 2.1 Introduction

### 2.1.1 Biological background

Cellular trafficking is an important process a living cell relies on to survive and communicate with other cells in the environment. A widely utilized form of cellular trafficking is cellular budding characterized by the local protrusion on a cell surface that results in a new vesicle separated from the cell surface it originates from. Many forms of cellular budding exist, and can work under very different mechanisms. In this chapter we focus on the nanometer length scale case, such that the cellular budding is not related to cell growth

but a local protrusion on a cell surface. At this length scale, cellular budding often takes the form of endocytosis. Endocytosis is a biological process best described as the cellular uptake of nanoparticles which are the nanometer scale aggregates of biological molecules. Representative subtypes of endocytosis include the particle-devouring phagocytosis, the lattice-building clathrin-mediated endocytosis, the ligand-binding receptor-mediated endocytosis, and lipid-mediated endocytosis. In addition, new endocytic pathways such as recently discovered fast endocytosis and ultrafast endocytosis [28, 56, 112] also exist. Endocytosis is not only utilized by cells to acquire nutrients, it is also used for synaptic transmission between neuron cells to exchange information. Furthermore, studies are being conducted on getting better understanding of endocytosis to help with designing an efficient method for drug delivery and shedding light on the biology of malignant cells to improve cancer treatments [75, 77, 93].

On the other hand, viral infection of a healthy cell is a prime example where endocytosis is utilized for cellular entry. Some viruses such as the alphavirus utilize the lipid-mediated endocytosis [28], while HIV-1 utilizes the receptor-mediated endocytosis [90]. After a virus successfuly infects the cell and undergoes viral reproduction, new viruses need to be released from the host cell to the environment. This is often done via two distinct methods: burst of the host cell and viral budding. Viral budding is a virus-releasing process that is comparable to endocytosis. The process initializes from the interior of the cell and the vesicle produced is released into the exterior environment. Virus can start as an assembled "core", a closed shell containing genetic information, in the cytosol of the host cell. The viral core travels toward the cell membrane and uses the endocytosis

process to exit the host cell [81]. Alternatively, virus can be formed from individual proteins carrying genetic information in the cytosol that travel and aggregate on the cell membrane to form a protruding vesicle [14, 107]. In fact, both exiting mechanisms are analogous to the lipid-mediated endocytosis and the clathrin-mediated endocytosis, but with the exterior environment of the cell as the final destination.

The cell membrane in the form of a double-layered thin sheet, often called the lipid bilayer, plays an important role in endocytosis. Properties of the cell membrane are heavily influenced by its biochemical composition; different properties would arise from different concentrations of the intra-membrane molecules. Under the normal circumstance a cell membrane exists in the so-called liquid-disordered phase that favors membrane-bound diffusion and membrane fluctuation. The cell membrane can also undergo rapid biochemical change by increasing the concentration of glycoproteins and cholesterols, which leads to structural change in the packing of intra-membrane molecules. For instance, upon the increase in the concentration of cholesterol, the ordering of the membrane molecules transforms into a well-ordered state giving rise to the "membrane raft", restuling in increased bending rigidity of the membrane [46, 99, 62].

Aside from the bending rigidity, an equally important property of the cell membrane is the membrane fluidity (viscosity). The concept of membrane fluidity is best understood as the ability to adapt to drastic geometric deformation, allowing a cell to generate many different shapes. In the next section we will discuss the computational modelling approaches centered around the general endocytosis and viral budding.

## 2.2 Modeling and method

### 2.2.1 Modeling background

Many researchers have focused on developing accurate and efficient representations of the cell membrane in different spatial scales. At the all-atomic level, model frameworks such as CHARMM, AMBER, Slipids, and GROMOS describe the cell membrane with detailed representation of lipid molecules, intra-membrane proteins, and water molecules surrounding the membrane, and are sufficiently general for a complex simulation [71]. At the (supra-) coarse-grained level, Cooke et al. [21] developed a coarse-grained self-assembled implicit solvent model based on the collective behavior of multiple linked beads as a generic representation of the lipid-bilayer. In their model, water molecules are no longer explicitly represented. A similar model independently proposed by Brannigan et al. [11] incorporates the same particle-based approach with different number of linked particles representing each individual lipid molecule. In both the all-atomic model and the (supra-) coarse-grained model described here, the membrane is represented as a two-layered system of linked beads. The key feature of these membrane models is that the general membrane behavior is determined via the attractive-repulsive interaction, such as the one described by Morse potential, between different beads. In [21], albeit within very specific ranges, experimentally relevant values of bending rigidity of the lipid bilayer are obtained. In their setup, the bending rigidity is controlled by the maximum range of molecular interactions between tail beads of the coarse-grained lipid molecules. Adopting the model developed by [21], Ruiz-Herrero et al. [95] studied the mechanism of budding of nanoscale particles and proposed a minimal model producing results in agreement with the elastic theory. Similar studies were

performed by Gao et al. [33] and Spangler et al. [105], with their own modifications of the implicit solvent model, to investigate the budding of nanoparticles with different forms of adhesive interactions and particle sizes.

In addition to the two-layered implicit solvent models, one-layer membrane model has also been developed and widely utilized. Major setups for the one-layer membrane model include interacting spheres and are similar to the implicit solvent model described earlier, and involve triangulated surface type. For interacting spheres type model, Feng et al. [31] proposed a one-layer model which takes 3D blocks of the model membrane in the all-atomic model and the implicit solvent model and simplifies these blocks into interacting spheres. In his work, the nature curvature of the membrane is described via the angle between the vertical axis of interacting spheres. For triangulated surface type model, Kohyama et al. proposed a Monte Carlo based simulation with the tether-and-beads triangulated mesh for crystalline budding process [60] which utilizes bond-flipping algorithm to represent the fluidity of the membrane. In the triangulated surface model, membrane curvature can be described in many different methods, and the choice often depends on the exact construction of the model.

Nanoparticle wrapping process has been studied extensively in 2-dimensional setup. The elastic theory is a well-studied and extensively developed subject. Researchers including Raatz et al. [94] and Yi et al. [115] have all provided comprehensive studies on budding and endocytosis, with models not restricted to rigid spherical nanoparticles, resulting in valuable conclusion on conditions affecting the theoretical predictions.

### 2.2.2 Model description

Our choice of coarse-grained particle-based membrane model is based on the discretized triangulated 2D surface embedded in 3D domain. In our model the particles (nodes) are connected via linear springs and the bending angle between any two edge-neighboring triangles is determined by the dihedral angle of the outward normal vectors. Nodes not connected within mesh also interact with each other through volume exclusion.

The initial configuration is a flat sheet with triangulated hexagonal meshes. The membrane model aims to capture the basic and yet important elastic characteristic cell membrane. Membrane mechanics are described by the energy potentials associated with various membrane properties. For each node in the triangular mesh, to maintain the discrete size of the triangular mesh, a preferred equilibrium length between the nodes is prescribed. In this representation, the membrane would respond accordingly to lateral compression or extension. Because such reaction is linked to the level of lateral deformation, it is described using the simple linear spring potential which is suitable for small perturbation.

$$E_{lin-sp} = \frac{k_s}{2}(R - R_0)^2 \tag{2.1}$$

Like the triangulated mesh proposed by Okuda and Eiraku [85], each individual triangular element comprises a constant number of membrane molecules. Deformation of a triangle, in this setup, represents the change in the geometric arrangement of the lipid molecules. Between any two unlinked nodes, the universal volume exclusion is applied to prevent self-intersecting. The curvature of the surface can be represented using $\sin(\theta/2) = (12C_0^2/R_0^2 - 3)^{-1/2}$, where $C_0$ is the radius of curvature, as introduced in Zandi et al. work on virus capsid assembly [111]. The bending is chosen to be modeled by the cosine angle

potential based on the dihedral angle between adjacent triangles.

$$E_{bend} = k_b(1 - \cos(\theta - \theta_0)) \tag{2.2}$$

$$= k_b\Big(1 - \frac{N_1 \cdot N_2}{|N_1||N_2|}\cos(\theta_0) - \Big(\frac{N_1 \times N_2}{|N_1||N_2|} \cdot \hat{ud}\Big)\sin(\theta_0)\Big) \tag{2.3}$$

The cosine angle potential is rewritten using the cosine identity into the dot product and cross product representation. Here $\hat{ud}$ is the normalized vector representing the edge shared by two triangles with specific orientation. This expansion of the cosine angle potential is important since the derivative of $\theta$ would lead to differentiation of $\arccos(*)$ where the singularity arises when the unit normal vectors of two triangles are parallel.

Due to the incompressibility of the membrane, the surface elastic energy of each individual triangular facet is described using a harmonic potential. This in conjunction with the cell volume mentioned earlier controls the in-plane elasticity of the model membrane. Imposing the incompressibility condition also leads to the conservation of the number of membrane molecules per triangular element [85].

$$E_{area} = \frac{k_a(A - A_0)^2}{2A_0} \tag{2.4}$$

Interaction between the membrane and another object can be described by, if such interaction involves adhesion-repulsion relationship, the standard 12-6 Lennard Jones potential. 12-6 Lennard Jones potential is the case of the general 2n-n Lennard Jones potential with $n = 6$.

$$E_{adh} = \epsilon\Big(\Big(\frac{R_{min}}{R_{ij}}\Big)^{2n} - 2\Big(\frac{R_{min}}{R_{ij}}\Big)^{n}\Big) \tag{2.5}$$

Since the model is applied to modeling adhesive interactions resulting in the adherence of the model membrane to the target particle, it is possible that different domains

on the model membrane may come into close contact. To prevent membrane crossing, self-avoiding property is imposed in the form of Morse potential:

$$E_{vex} = k_{vex}\Big(1 - \exp(-\alpha(R_{ij} - R_0^{vex}))\Big)^2 \tag{2.6}$$

Based on the potential energies associated with different membrane characteristics, we can describe the dynamics of the system by accounting for all energies present in the system:

$$E_{total} = \sum E_{lin-sp} + \sum E_{bend} + \sum E_{area} + \sum E_{adh} + \sum E_{vex} \tag{2.7}$$

### 2.2.3 Membrane-particle interaction

As described in the membrane model, the solid (or elastic) particle representing the viral capsid shell interacts with the membrane through $2n - n$ Lennard Jones potential. The viral capsid shell can be represented as a rigid spherical object, an infinitely stiff solid particle built from aggregated sub-particles, or a soft elastic solid particle.

In the case of an elastic solid particle case, another set of parameters for equilibrium bond length, preferred bending angle, and area conservation constraint is required Given different parameter values, the interaction between the cell membrane and the elastic particle of different rigidity can be simulated.

We investigated the scenario where the budding nanoscale particle is a rigid sphere. The interaction range is defined to be $\alpha + R_0$ where $\alpha$ is the radius of the particle and $R_0$ is the thickness of the membrane.

### 2.2.4 Membrane fluidity (viscoelasticity)

The exact concept of membrane rigidity is a tricky matter. Because plasma membrane is capable of in-plane reorganization of membrane molecule, the effective rigidity cannot be represented by a simple bending coefficient. It is well established that the plasma membrane can have different compositions thus the resulting mechanical properties are different. One particularly well known contribution is the cholesterol, which accounts for approximately 30% of the plasma membrane, such that its concentration directly influences the membrane "stiffness" [91]. Several experiments also focused on the effect of depletion or enrichment of the cholesterol. For instance, noticeable influences were observed on the interaction between a cholesterol concentration altered plasma with an external components such as viral proteins and cytoskeleton [106, 43]. Hence, in addition to the standard approach for establishing a membrane model, a combination of components involving some forms of bending coefficient, stretching coefficient, and area incompressibility, the fluidic nature of the membrane must be modeled as an adaptive process reacting to external or internal stimuli.

There are in general two approaches to model the fluidity (viscoelasticity) of the membrane. The difference depends on whether the mesh of the membrane maintains initial connectivity or it is updated dynamically. For the maintenance of the initial connectivity of the mesh, Maxwell model and Kelvin-Voigt model are often used. The two models can be described as a sequentially connected or parallelly connected linear spring and damping (viscosity) spring, respectively. These models ensure that the mesh, or the system it is trying to mimic, does not respond to stress elastically. The damping (viscosity) term aims

to increase resistance when the stress is continuously applied and impede relaxation when the stress is removed.

The Monte Carlo method for the edge re-connectivity is a well-established approach which has been shown to effectively capture the topological change of the plasma membrane. The fluidity is represented by a rearrangement of the triangular network through cutting an existing bond and establishing a new bond between nodes [40, 1]. Using this approach, the membrane fluidity is therefore characterized by the introduction of non-hexagonal polygons which have non-trivial curvatures.

We choose the metropolis algorithm for bond-flipping probability computation due to its simplicity and fulfillment of the detailed balance condition, such that the traverse between different states of connectivity is reversible. Hence, given a pair of edge-sharing triangles, $\Delta_{j,k,l,i}$, the probability that edge $e_{ik}$ would be cut and re-establish as $e_{jl}$ is

$$P(e_{jl}|e_{ik}) = \left\{1, \exp\left(\frac{-(E_{e_{jl}} - E_{e_{ik}})}{\omega}\right)\right\} \tag{2.8}$$

where $E_{e_{ik}}$ and $E_{e_{jl}}$ are the local energies in the system pre-bond-flip and post-bond-flip states, respectively. $\omega$ has the unit of energy and determines the acceptance probability. When $\omega$ increases (such as in case of an increase in temperature when $\omega = k_B T$), it leads to increased fluctuation. Increased acceptance probability leads to the scenario where the topology of the system is more prone to change. Decreased acceptance probability results in reduced fluctuation.

This re-meshing approach represents the tendency of lipid molecules to experience in-plane reorganization. When the acceptance probability is sufficiently low, minimal

movement of lipid molecules would be observed as if the membrane is similar to a solid material.

**Computational implementation of the edge-reconnectivity algorithm.** The edge-reconnectivity algorithm described earlier can be understood as traversing through a state space searching for particular edge-connectivity that allows the current system to better approach the target shape. Consider a triangulated 3D surface with $N$ edges, the initial edge-connectivity serves as state $S_0$. If we choose one of the edges and switch the connectivity within the subsystem, a new state is generated. This implies that there exists $S_1, S_2, \cdots, S_N$ states that are connected to $S_0$. For state $S_i$, the same idea can be applied such that $S_{1,1} = S_0, S_{1,2}, \cdots, S_{1,N}$ are the states connected to $S_1$. This process can be repeated indefinitely since for every edge-reconnectivity applied, new states can be generated accordingly. Note that in this the detailed balance can be achieved, namely that for any two states $S_{a_1,a_2,\cdots,a_N}$ and $S_{b_1,b_2,\cdots,b_N}$, there exists a mutual path, albeit such path is not unique and multiple paths can exist.

**Model representation of membrane fluidity.** In the particle-based model, the viscosity of the membrane is represented by the strength of adhesive interaction between molecules. Stronger interaction leads to lower fluidity (i.e. higher viscosity) that impedes the membrane deformation. In the lattice based model without considering bond breakage (i.e. deletion of an existing edge), the membrane fluidity can be understood as the efficiency of the current lattice achieving lower energy state through several attempts of re-meshing algorithm. Hence, one can computationally capture the membrane fluidity by controlling the frequency or the likelihood of the accepted reconnectivity. In this setup, the lower the

frequency or likelihood of accepting a proposed reconnectivity, the less likely the current mesh will evolve to a configuration that gives a lower energy state.

In this chapter, we utilize two different forms of membrane fluidity. We vary the acceptance probability by either changing the size of sampling for bond reconnectivity attempts or artificially changing the acceptance probability (resulting in the increased and decreased fluctuation) while the number of bond flip attempts is fixed. In both cases, the endocytosis process has been shown to be affected by the membrane fluidity.

### 2.2.5 Simulation method

The choice of position update scheme of the nodes depends on the type and goal of the simulation. For a non-equilibrium system evolution, methods such as the explicit Euler, implicit Euler and velocity Verlet algorithm are good candidates. Methods such as the Gradient descent and quasi-Newton BFGS update are more suitable for searching of the equilibrium configuration of the system.

In this thesis, we chose to employ the forward Euler scheme. Motion of each node is described using the following equation:

$$c\dot{x_i} = -\nabla_{x_i} E_{total} \tag{2.9}$$

$$x_i(t+1) = x_i(t) + \dot{x}_i(t)\Delta t \tag{2.10}$$

where c is the friction term depicting the viscosity of the system. This method is analogous to the steepest descent method in optimization theory. Hence, based on energy dissipation, the system will relax to a locally minimal energy state. The force is computed analytically to avoid the approximation error risen from numerical differentiation.

Model simulations are performed as follows:

1. Initialize the mesh of the system, data structures and parameters. Data structures of the system include the information on:
   (a) X-, y-, and z-coordinates of each node in the mesh
   (b) Indices of the two nodes of each edge
   (c) Indices of the three nodes of each triangle
   (d) Indices of the three edges of each triangle
   (e) Adjacency of triangles in the mesh
   (f) Adjacency of nodes in the mesh
2. Apply forward Euler method to update each node position up to N steps.
3. Randomly sample a pre-determined number of edges to perform Monte Carlo bond flip algorithm. Update the data structures in step 1 accordingly.
4. Repeat step 2 and 3 until simulation time expires (MD) or convergence is observed (MC).

The model implementation was initially prototyped using MATLAB and has been ported to C++. The MATLAB code was parallelized to improve performance, but it became inefficient when the mesh size exceeds 200 nodes. Furthermore, the edge re-connectivity algorithm necessary for representing the membrane fluidity proved to be the most time consuming operation. Hence the MATLAB code is converted into C++ code with implementation on a GPU (graphic processing unit) computing platform with the help of Samuel

Britton. GPU implementation was at least 100-fold faster than the MATLAB implementation. The C++ version of the code can be found on github and the link is provided in the previous chapter. The code has been modified to incorporate cell growth algorithm but can be easily changed to disable the growth algorithm for nanoscale budding simulation.

## 2.3 Model validation

### 2.3.1 Viscoelastic properties

As described in the earlier section, viscoelasticity is an important property of the cell membrane. When cell membrane is under non-vanishing stress, its viscoelastic property allows the membrane to reduce total energy through restructuring molecular ordering.

To demonstrate and verify the membrane viscoelastic properties, we used a mesh with identical width and length. A pair of parallel boundaries were fixed and a gravitation-like force in the x-direction $F = (g, 0, 0)$, where $g$ is the constant force acting on each node, to induce an in-plane flow [83, 96]. When the membrane is given zero bond flip attempt, the solid-like behavior, characterized by the increase in the total energy of the system due to induced strain, is immediately observed. Another test is performed where the frequency of bond-flip is set to three attempts per fifty numerical integration time steps. The membrane is able relax to a lower energy state with resulting mesh profiles mimicing the 2D Poiseuille flow (Figure 2.1).

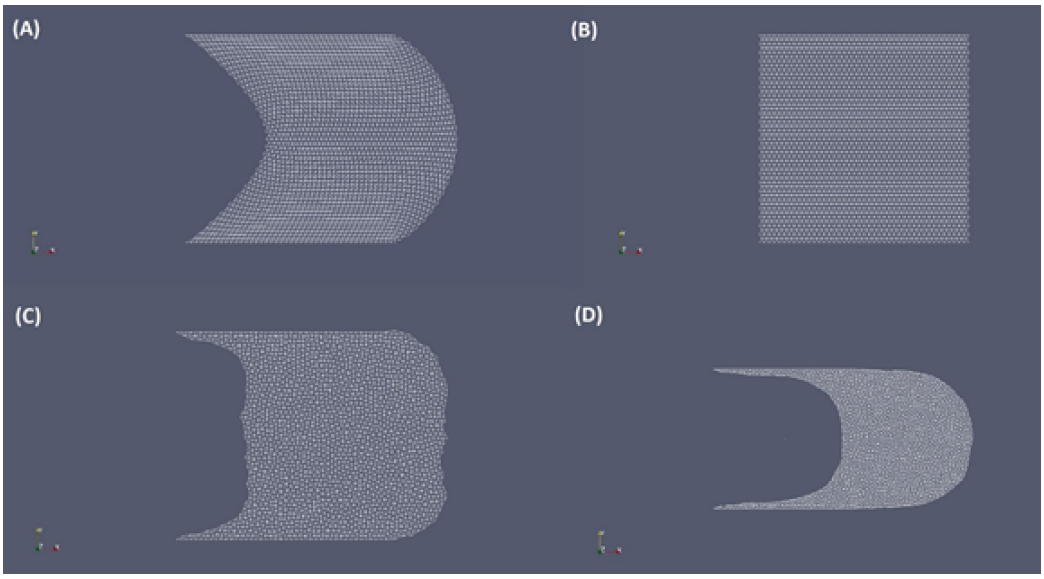


Figure 2.1: Influence of membrane fluidity in response to in-plane flow. (A) The steady-state of the solid-like system under flow. (B) Initial configuration of the fluidic system. (C) Snapshot of the fluidic system under in-plane flow. Note the change in topology allows the system to make adjustments. (D) The Poiseuille flow profile after extended simulation time. The configuration of the system shows the parabolic shape indicating the maximum velocity occurring along the central line in the x-direction.

### 2.3.2 Monte Carlo energy minimization

**Brief review of the theory of icosahedral symmetry.** A typical vesicle formed during the endocytosis process is spherical. If a triangulated spherical surface is built by equilateral triangles, the number and arrangement of pentagons and hexagons, formed using these triangles, are determined by the Euler characteristic. In what follows we review definitions and formula related to the Euler characteristic (for example see [57]).

**Definition 1** *A* **polyhedron** *is a three-dimensional solid with flat polygonal faces, straight edges and edge-joining nodes.*

**Definition 2** *Given a surface of polyhedra, the* **Euler characteristic** $\xi$ *is defined as* $\xi = V - E + F$*. Here* $V$*,* $E$ *and* $F$ *are the number of nodes, edges and faces, respectively.*

**Theorem 3** *(Euler's polyhedron formula) Let $M$ be a convex polyhedron. The Euler characteristic of $M$ must satisfy the condition $V - E + F = 2$.*

If we assume that such convex polyhedron consists of only regular pentagons and regular hexagons, the Euler's polyhedron formula can be rewritten as

$$V - E + P + H = 2 \tag{2.11}$$

where $P$ and $H$ are the number of pentagons and the number of hexagons. In addition, since each pentagon and hexagon have five and six edges respectively, this implies that

$$2E = 5P + 6H \tag{2.12}$$

$$V - \frac{5P + 6H}{2} + P + H = 2 \tag{2.13}$$

$$\Rightarrow V - \frac{3P + 4H}{2} = 2 \tag{2.14}$$

Similarly, the number of nodes can also be represented by $P$ and $H$ with the constraint such that each node can only be shared by three polygons. This means that

$$3V = 5P + 6H \tag{2.15}$$

and

$$\frac{5P + 6H}{3} - \frac{3P + 4H}{2} = 2 \tag{2.16}$$

$$\Rightarrow \frac{P}{6} = 2 \tag{2.17}$$

$$\Rightarrow P = 12 \tag{2.18}$$

Hence, to form an approximation of a spherical vesicle composed of regular pentagons and regular hexagons, Euler's theorem requires exactly 12 pentagons (also called

five-fold disclinations). The necessity to have pentagons distributed over the surface is for accommodations of nontrivial curvatures. Given only regular hexagons, the minimal energy structure achieved would be a flat surface. Using similar argument presented above one can easily deduce that if only regular hexagons are allowed, the Euler's characteristics formula would give the following result:

$$V - E + F = 2 \tag{2.19}$$

$$\Rightarrow 2H - 3H + H = 2 \tag{2.20}$$

$$\Rightarrow 0 = 2 \tag{2.21}$$

which is a contradiction. This can also be observed by representing regular pentagons and regular hexagons using equilateral triangles. In this representation, each hexagon must remain flat such that the interior angle maintains 360 degrees. However in the case of pentagon, a nontrivial curvature must exists since the interior angle is only 300 degrees.

**Model validation using simulated annealing** The minimal energy state of such vesicle also requires a specific positioning of the pentagons. For example, the truncated icosahedron (or the soccer-ball) with 80 equilateral triangles must have specific arrangements as presented in Figure 2.2 and Figure 2.3. This is the icosahedral symmetry when the spherical shell is constructed purely by pentagons and hexagons.

To ensure that the membrane fluidity in our model is both physically and statistically plausible, we solved the energy minimization problem for icosahedrons of various size. We used the phase diagrams introduced by by Wagner et al. and Panahandeh et al. [111, 88] along the indicated parameters to test whether our formulation can also lead to the minimal energy structure. An annealing step is applied to ensure that the sequence

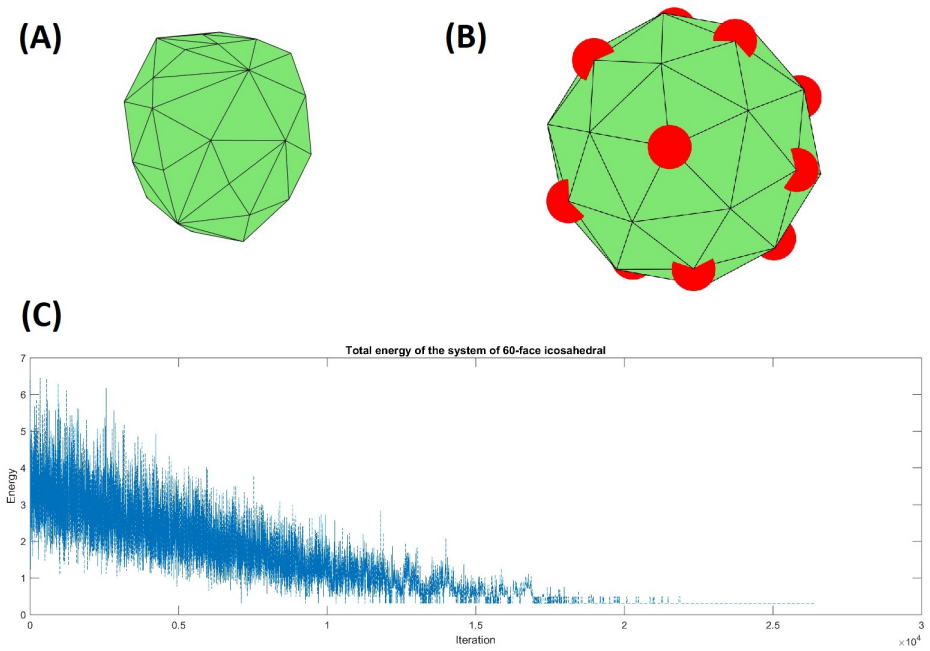


Figure 2.2: Energy minimization of a polyhedron composed of 60 triangles. (A) Initial configuration. (B) The red dots indicate the positions of each pentagon. (C) Evolution of the total energy of the system under simulated annealing method.

of generated structures can converge to the minimal structure configuration. The annealing process involved a monotonically decreasing nonlinear sequence of $\omega$ values such that $\{\omega\}_{j+1} = 0.9 \cdot \{\omega\}_j$. For each $\omega$ value, we performed 1000 bond-flip grand attempts where each single grand attempt consisted of N single bond-flip attempts.

We simulated all sizes of the icosahedral presented in the [111, 88] to validate fluid type behavior of the model. Based on the qualitative observations, the obtained results are in agreement with the results described in previous papers. In addition, from the energy perspective the system also achieved the minimal energy states.

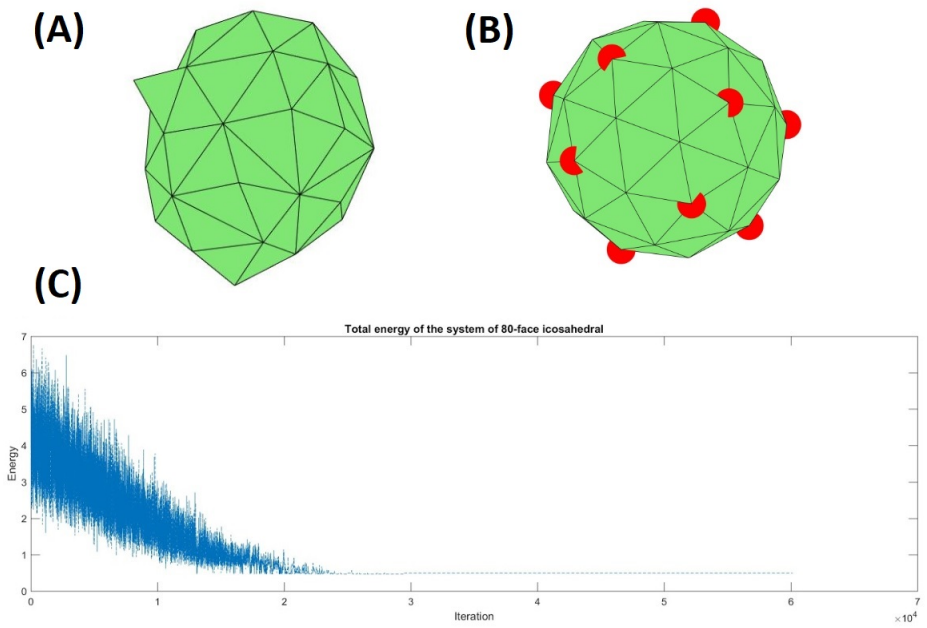


Figure 2.3: Energy minimization of a polyhedron composed of 80 triangles. (A) Initial configuration. (B) Global minimal energy configuration. The red dots indicate the positions of each pentagon. (C) Evolution of the total energy of the system under simulated annealing method. Notice that the number of sampling needed is higher than the case with 60 triangles in Figure 2.2 due to the increased complexity of the configuration.

## 2.4 Cell budding and endocytosis

### 2.4.1 Comparison with existing models and theoretical predictions

According to the elastic theory, the final shape obtained as a result of budding and endocytosis process depends on the ratio of the bending stiffness to the adhesion strength between the membrane and the particle. In the context of energy minimization, under the assumption of ideal membrane fluidity, the degree of wrapping of the particle is determined directly by the difference in the speed of relaxation of the bending energy and the adhesion energy. Because the dynamics of each component in the model is based on energy dissipation, naturally it becomes a competition between different components trying to reach equilibrium.

Many models developed for the budding and endocytosis process give rise to comparable results in terms of the degree of wrapping and the neck profile of the budding site. For instance, Raatz et al. [94] suggested that given a fixed membrane bending stiffness, different adhesion energies produces different minimum-energy profiles (Figure 2.4). By choosing a fixed adhesive interaction range $\rho$, a general pattern of the phase transition can be identified as a sigmoidal curve. The ratio between the adhesion energy and the degree of wrapping not only resembles a sigmoidal curve, it also shows a convergence toward sharp transition between a unbounded nanoparticle and a fully wrapped nanoparticle. Model described in this Thesis also captures this sigmoidal profile which is qualitatively similar to the cases with $\rho = 0.1R$ and $\rho = 0.01R$ where $R$ is the radius of the nanoparticle.

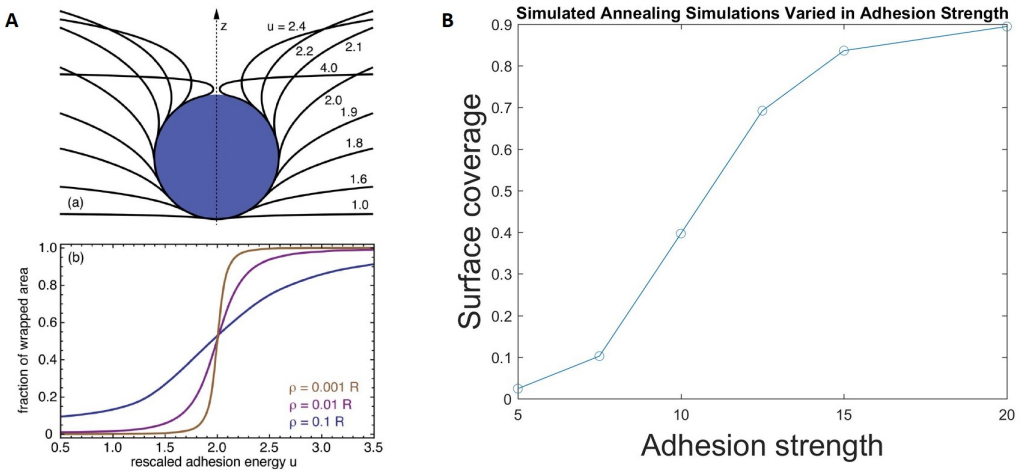


Figure 2.4: Comparison between simulation result of our model and existing theoretical predictions. (A) Prediction of the nanoparticle wrapping by different values of adhesive strength and range of interaction [94]. (B) The simulated result of our model for a chosen set of parameters including the membrane stiffness and adhesive interaction range. The sigmoidal curve matches qualitatively to the theoretical prediction.

Another comparison we made involves the budding neck profile. In both elastic theory calculations and the numerical simulations by Ruiz-Herrero et al. [95], it is observed that for the range of adhesive strength that can induce complete wrapping, the difference in the magnitude gives rise in the different budding neck profiles. The budding neck magnitude is higher when the adhesive strength is lower and vice versa. This follows from the fact that stronger adhesive strength leads to faster relaxation of the adhesive interaction between the membrane and the particle. We also observed this behavior in our model simulations (Figure 2.5).

### 2.4.2 Influence of membrane fluidity on budding and endocytosis

Our model Monte Carlo statistical (simulated) annealing simulation have demonstrated the ability to produce qualitative, and to a lesser degree quantitative, result com-

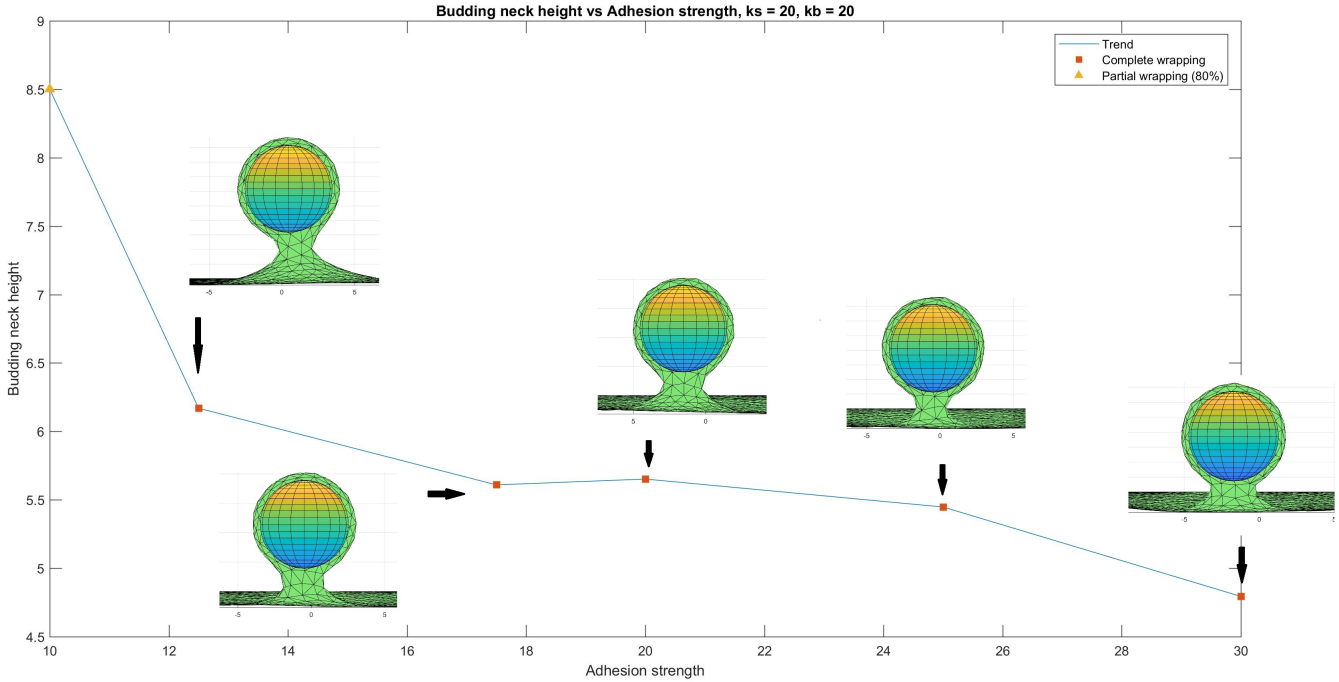


Figure 2.5: The budding neck profile based on different adhesive strengths. The cross-sectional views are the configuration shortly before complete wrapping happens. As the adhesive strength increases, the length of the budding neck shortens.

parable with the results obtained using existing models. However, as discussed in earlier section, that the annealing process is a method designed for the search of global minimal energy structure but it does not capture the actual evolution of the system. We are particularly interested in this Thesis in how fluidity of the membrane may influence the outcome of the nanoparticle wrapping.

As described before, when the system is under increased fluctuation condition, the probability of bond flip acceptance increases. The simulation results showed that the degree of wrapping increases with increased acceptance probability as in the case of increased temperature (Figure 2.6). We further investigated the influence of the membrane fluidity (via increased and decreased fluctuation) on the transitions between unbounded state, partially wrapped state and completely wrapped state. We hypothesized that membrane fluidity would have catalyst-like effect that facilitate complete wrapping or at least improve the degree of wrapping for scenarios with low level of adhesive strength. Our simulation results suggest that membrane fluidity indeed promotes the transition from partially wrapped state to completely wrapped state in some cases. In addition, when the adhesive strength is sufficiently low, the membrane fluidity fails to promote wrapping process (Figure 2.7). Upon further examination of this phase diagram, it becomes clear that when the membrane fluidity is sufficiently high, only two states exist: complete wrapping state and minimal (or unbound) wrapping state, which agrees with the qualitative results of the existing model [94, 95]. Lastly, when the membrane fluidity is sufficiently low, we anticipated that no complete wrapping can be reached since the cell membrane would exhibit solid-like property

resisting drastic deformation. Our simulation results also agree with this prediction and we only observed the transition between minimally wrapped state and partially wrapped state.

### 2.4.3 Impact of membrane fluidity on particle wrapping efficiency

In this section, we investigate the effect of membrane fluidity on particle wrapping efficiency during the endocytosis process. Membrane fluidity in this section is determined by the size of sampling used for the edge reconnectivity [83]. Namely, the membrane fluidity depends on the number of edge sampled during the edge re-connectivity algorithm while the acceptance probability remains fixed. In these simulations the total simulation time is set to be $T = 50s$ while each individual time step is $\Delta t = 0.0005s$. The choice of timescale is based on the observed time of a typical clathrin-mediated endocytosis event. However, it is worth noting that the duration of endocytosis varies significantly, from tens of milliseconds to several minutes for different cell types and the subtypes of endocytosis [100]. To test different membrane fluidity, we used the following sample sizes: $\Phi = 0.1\%, 0.5\%, 1\%$. The strength of the membrane-particle adhesion described by the 6-3 Lennard Jones potential (with $n = 3$ for $2n - n$ relationship, see Section 2.2.2) was assumed to be $40, 80, 160 k_B T$. Furthermore, following setup similar to the one in Noguchi et al. [83], the edge re-connectivity algorithm was triggered every 20 iterative steps, to mimic molecular dynamics simulation. Lastly, we set the number of simulation per combination of $\Phi$ and membrane-particle adhesion strength to three to achieve increased statistical significance.

Simulation results show that when the mechanical properties of the membrane and membrane-particle adhesion strength are fixed, the membrane fluidity plays an important

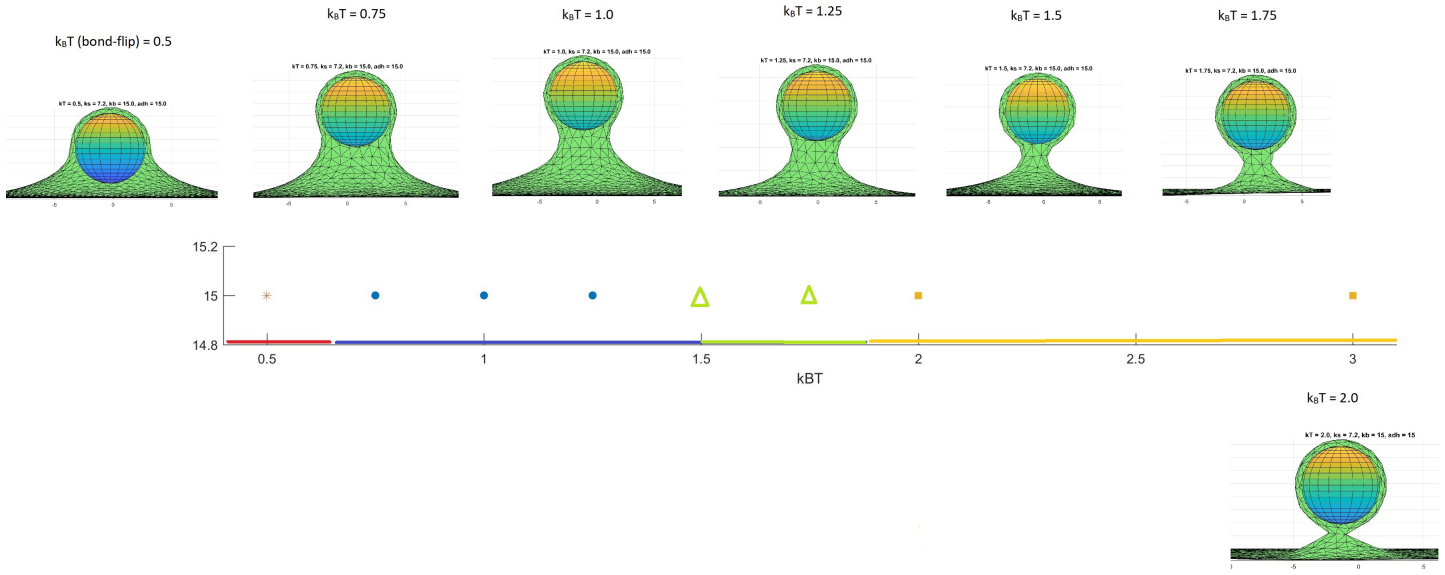


Figure 2.6: Influence of fluidity on the degree of wrapping. As the fluidity increases, the simulation result approaches complete wrapping state. There is a range of $\omega$ values that produces partially wrapped nanoparticle as a steady state.

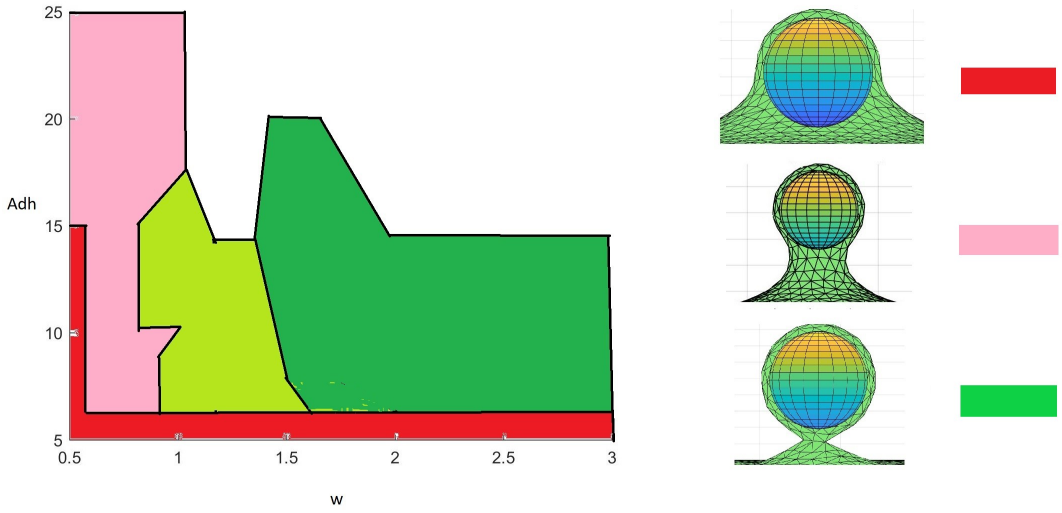


Figure 2.7: Phase diagram of the final wrapping state for different levels of membrane fluidity depending on system temperature. Red indicates unbounded or wrapping state with less than 50% surface coverage. Pink indicates the partially wrapped state with wrapping level ranging from 50% to 90%. Light green indicates fluctuation between the partially wrapped state and the completely wrapped state. Dark green indicates the completely wrapped state. The remaining white region is the untested parameter combinations. Here $\omega$ is in the unit of $k_BT$, and note that the value of $\omega$ is purely theoretical and is not corresponding to real temperature.

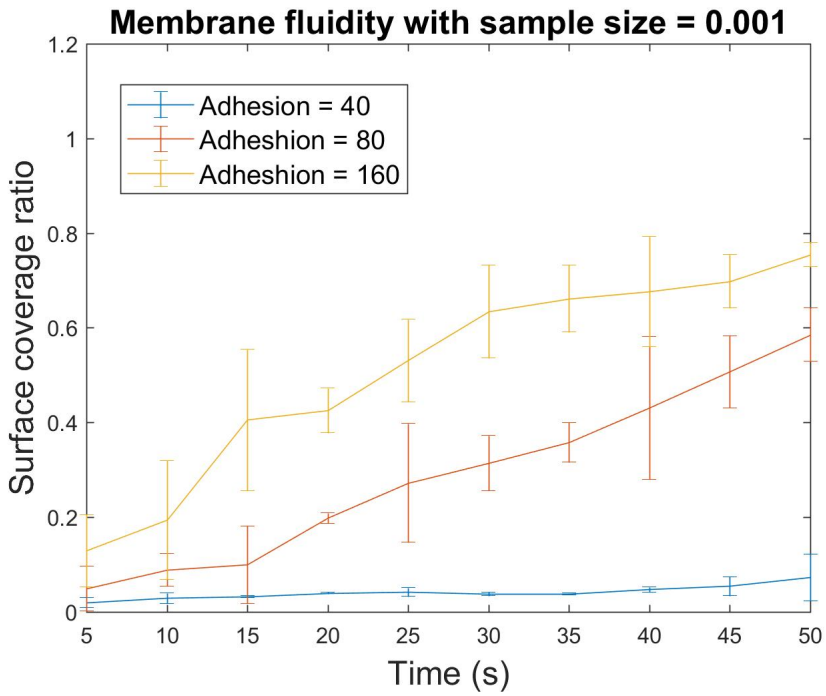


Figure 2.8: Surface coverage of the particle interacting with a cell membrane. The fluidity of the membrane is based on a sampling size of 0.1% of the number of non-boundary edges in the model membrane.

role in determining the degree of particle surface wrapping within the designated simulation time. In particular, the higher the membrane fluidity, more coverage of the particle by surface of the membrane can be achieved. Also, similar to the results presented in earlier section, increased membrane fluidity represented by more conventional algorithm, can improve the degree of wrapping even when the membrane-particle adhesion is lower. Figure 2.8 and 2.9 provide plots of the degree of wrapping of a particle by membrane quantified by the percentage of surface coverage of the particle.

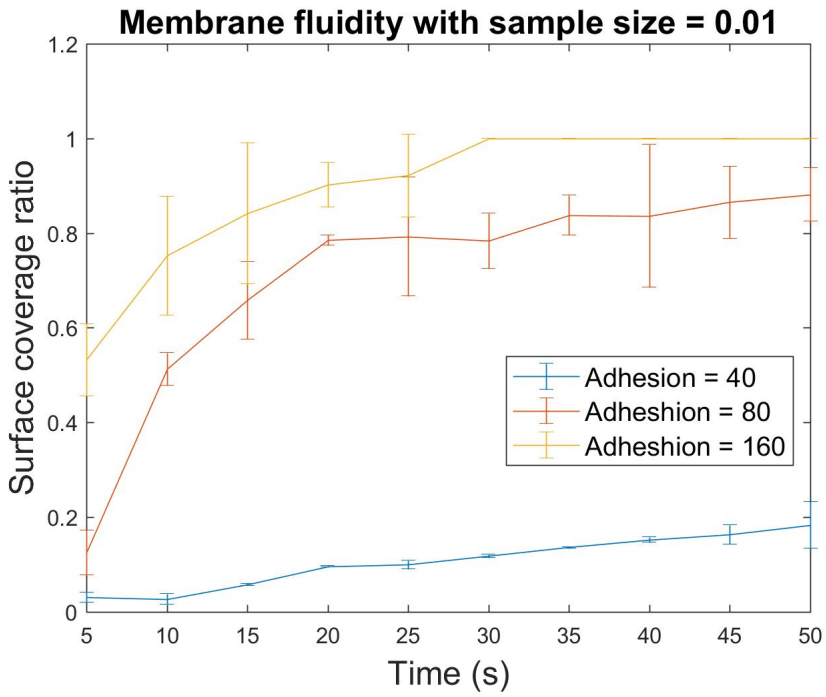


Figure 2.9: Surface coverage of the particle interacting with a cell membrane. The fluidity of the membrane is based on a sampling size of 1% of the number of non-boundary edges in the model membrane. Compared to membrane with lower fluidity, the wrapping process is overall more efficient such that it takes significantly less time to achieve 70% coverage for cases with adhesion strength of 80 and 160 (Figure 2.8).

### 2.4.4 Limitations of the current model

In the work of Raatz et al. [94], the authors investigated the influence of adhesive interaction range and concluded that shorter interaction range leads to sharper phase transition, i.e. short range of interaction causes a sudden jump from unbounded state to a complete wrapping state. This observation was also made in Cooke et al. [21] and Ruiz-Herrero et al [95]. where it was indicated that simulation results converge to either an unbounded state or completely wrapped state under the assumption that the adhesive interaction being relative short.

Since our model is based on surface triangulation, there is a lower bound on the adhesive interaction range that can be prescribed. The lower bound value depends on the chosen size of the mesh. The minimal range to induce any meaningful interaction must be roughly $\sqrt{3}R_{min}$ where $R_{min}$ is the equilibrium length of the edge in the system. This implies that our model is not suitable for studying problems at molecular and sub-molecular level, instead the model was designed for studying problems at mesoscale level.

### 2.4.5 Future model development

While the limitation of the current model prevents potential studies involving range of adhesive interactions between the nanoparticles and the cell membrane, several important biologically relevant problems can be investigated without explicit specification of the range of adhesive interactions. The early reproduction of the HIV-1 virus and the infection process of the alphavirus both require the presence of the membrane raft structure on the cell membrane, which is known to have increased bending rigidity but retain fluddity

[46, 99, 62, 86]. Whether the size of the raft structure is predetermined or dynamically enlarging and how such size may impact the budding process is yet to be determined. Furthermore, the existence and contribution of the line tension, the tendency of minimizing the contact length between membrane raft and normal membrane, are still widely debated among researchers. Our model can describe multiple domains with different mechanical properties representing membrane rafts and normal membrane. The model can also be used to study the influence of raft size on the exiting pathway of HIV-1 virus and the entry pathway of alpha virus.

Because our model uses a 3D coarse-grained triangulated mesh, the simulation time is shorter compared to the all-atomic models and implicit solvent models. This implies that we can introduce nanoparticles as aggregates of smaller spherical particles to represent different shapes. The rigidity of a nanoparticle can then be described via the interaction between the smaller spherical particles. It is important to study different shapes of the nanoparticles, particularly in the field of medicine, to better understand a more efficient drug deliver method. For example, what shape should the nanoparticle take to improve its entry into the cell? On the other hand, many questions involving shape of a nanoparticle are important in studying viral infection and reproduction as well. For instance, ebola virus is known to be a flexible tubule originated from the viral capsid proteins forming from multiple linked "cylindrical shells". It is still not well-understood how orientation of the tubule ebola virus with respect to the cell membrane can influence its entry into a cell. Also, it is not clear how virus is assembled, particularly why is there an advantage for the

cylindrical shells to approach the cell membrane perpendicularly or tangentially, during the reproduction stage.

## 2.5 Incorporating cell growth

While we already described cellular budding with cell growth in Chapter 1, in this section we will discuss this process using a different modeling approach.

At least three possible modeling approaches are suitable for describing localized cell growth:

1. The first approach is commonly used in the finite element method based models. Once the threshold value is reached, a new triangle is introduced inside an existing triangle. The nodes of the the new triangle are placed at the midpoints of the edges of the triangle it is embedded in. However, this approach is not compatible with the Monte Carlo re-meshing techniques for which curvature of the system is calculated based on bending angles between adjacent triangles. To utilize this approach, the model needs to be modified to eliminate the explicit use of bending energy potential.

2. Another approach is based on the addition of a new membrane node at the centroid position of the existing triangle. In this setup three new triangles are introduced. Computationally this is relatively less expensive and data structure manipulation is also relatively simple. From the topological point of view, this introduces an unfavorable configuration (3-fold disclination) which may lead to instability in a mechanical stress based model.

3. The last approach is introduced in [85] that the midpoint of a chosen edge is treated as a new membrane node. The two triangles sharing this edge are involved in calculations and new connections are established between this new node and the two opposite nodes that are not already connected with the midpoint. This approach is suitable for a mechanical stress based model where curvature is calculated using edges and bending angles are calculated using the unit normal vectors of each triangular facets. This is the approach adopted in Chapter 1.

The described approaches can be used in deterministic or probabilistic fashion. When used deterministically, the algorithm depends on factors such as the local area of the triangle and the applied stress. When used probabilistically, a probability distribution is calculated and used to determine the likelihood of membrane expansion. The distribution can be based on net change of energy of the system before and after the growth happens, or based on the current area of the triangles in the mesh.

## 2.6 Appendix

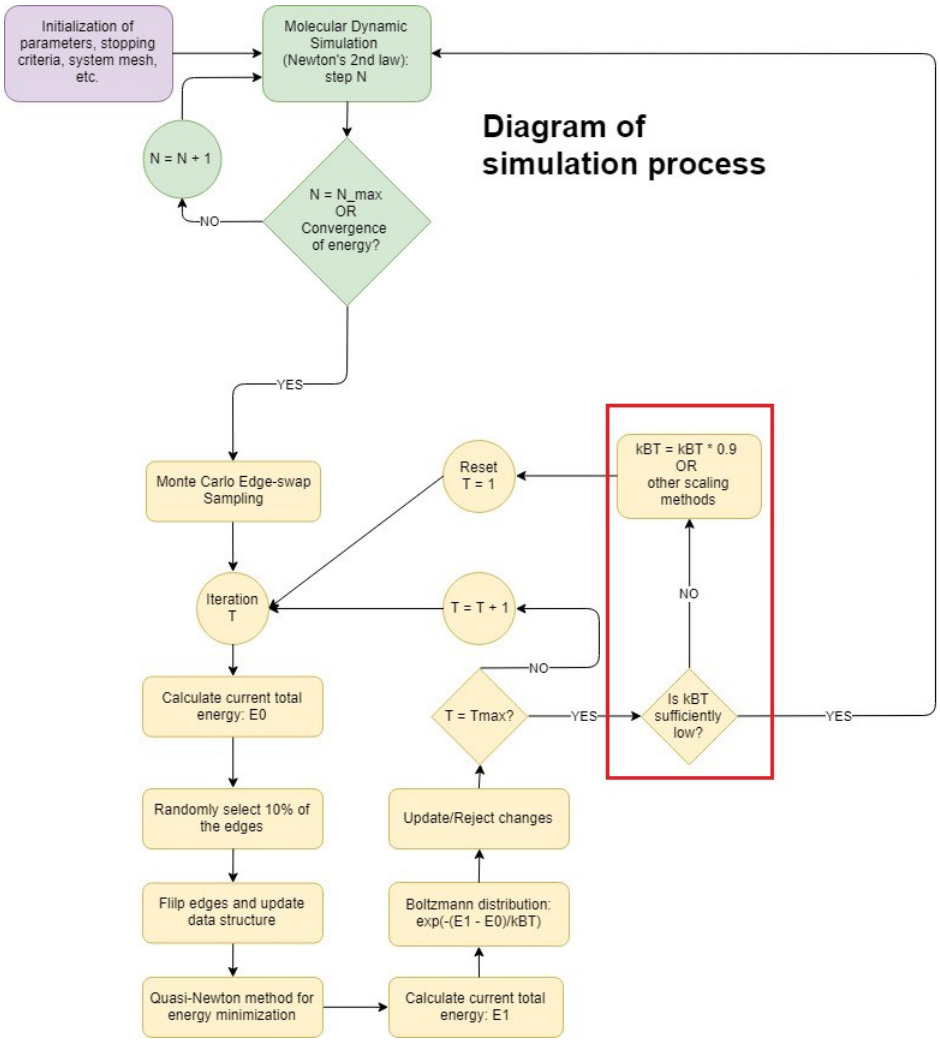


Figure 2.10: The diagram showing simulation process in both molecular dynamics and simulated annealing of virus budding and endocytosis. The red box indicates the steps that can be omitted if the simulation is molecular dynamics based.

# Bibliography


[1] Sanne Abeln, Michele Vendruscolo, Christopher M Dobson, and Daan Frenkel. A simple lattice model that captures protein folding, aggregation and amyloid formation. *PLoS One*, 9(1):e85185, January 2014.

[2] Tom Altenburg, Björn Goldenbogen, Jannis Uhlendorf, and Edda Klipp. Osmolyte homeostasis controls single-cell growth rate and maximum cell size of saccharomyces cerevisiae. *NPJ Syst Biol Appl*, 5:34, September 2019.

[3] K R Ayscough, J Stryker, N Pokala, M Sanders, P Crews, and D G Drubin. High rates of actin filament turnover in budding yeast and roles for actin in establishment and maintenance of cell polarity revealed using the actin inhibitor latrunculin-a. *J. Cell Biol.*, 137(2):399–416, April 1997.

[4] Amir H Bahrami, Michael Raatz, Jaime Agudo-Canalejo, Raphael Michel, Emily M Curtis, Carol K Hall, Michael Gradzielski, Reinhard Lipowsky, and Thomas R Weikl. Wrapping of nanoparticles by membranes. *Adv. Colloid Interface Sci.*, 208:214–224, June 2014.

[5] Samhita P Banavar, Carlos Gomez, Michael Trogdon, Linda R Petzold, Tau-Mu Yi, and Otger Campàs. Mechanical feedback coordinates cell wall expansion and assembly in yeast mating morphogenesis. *PLoS Comput. Biol.*, 14(1):e1005940, January 2018.

[6] Mikahl Banwarth-Kuhn, Ali Nematbakhsh, Kevin W Rodriguez, Stephen Snipes, Carolyn G Rasmussen, G Venugopala Reddy, and Mark Alber. Cell-based model of the generation and maintenance of the shape and structure of the multilayered shoot apical meristem of arabidopsis thaliana. *Bulletin of mathematical biology*, 81(8):3245–3281, 2019.

[7] Christian Bartels and Martin Karplus. Probability distributions for complex systems: adaptive umbrella sampling of the potential energy. *The Journal of Physical Chemistry B*, 102(5):865–880, 1998.

[8] Erfei Bi and Hay-Oak Park. Cell polarization and cytokinesis in budding yeast. *Genetics*, 191(2):347–387, June 2012.

[9] Noelia Blanco, Michael Reidy, Javier Arroyo, and Enrico Cabib. Crosslinks in the cell wall of budding yeast control morphogenesis at the mother–bud neck. *J. Cell Sci.*, 125(23):5781–5789, December 2012.

[10] Horst-Holger Boltz and Jan Kierfeld. Shapes of sedimenting soft elastic capsules in a viscous fluid. *Phys. Rev. E Stat. Nonlin. Soft Matter Phys.*, 92(3):033003, September 2015.

[11] Grace Brannigan, Lawrence C-L Lin, and Frank LH Brown. Implicit solvent simulation models for biomembranes. *European Biophysics Journal*, 35(2):104–124, 2006.

[12] Enrico Cabib and Javier Arroyo. How carbohydrates sculpt cells: chemical control of morphogenesis in the yeast cell wall. *Nat. Rev. Microbiol.*, 11(9):648–655, September 2013.

[13] Otger Campàs and L Mahadevan. Shape and dynamics of tip-growing cells. *Curr. Biol.*, 19(24):2102–2107, December 2009.

[14] Lars-Anders Carlson, John AG Briggs, Bärbel Glass, James D Riches, Martha N Simon, Marc C Johnson, Barbara Müller, Kay Grünewald, and Hans-Georg Kräusslich. Three-dimensional analysis of budding sites and released virus suggests a revised model for hiv-1 morphogenesis. *Cell host & microbe*, 4(6):592–599, 2008.

[15] Juliane P Caviston, Serguei E Tcheperegine, and Erfei Bi. Singularity in budding: a role for the evolutionarily conserved small GTPase cdc42p. *Proc. Natl. Acad. Sci. U. S. A.*, 99(19):12185–12190, September 2002.

[16] Hsin Chen, Audrey S Howell, Alex Robeson, and Daniel J Lew. Dynamics of septin ring and collar formation in saccharomyces cerevisiae. *Biol. Chem.*, 392(8-9):689–697, August 2011.

[17] Long Chen. iFEM. `https://www.math.uci.edu/~chenlong/programming.html`. Accessed: 2020-4-30.

[18] Weitao Chen, Qing Nie, Tau-Mu Yi, and Ching-Shan Chou. Modelling of yeast mating reveals robustness strategies for Cell-Cell interactions. *PLoS Comput. Biol.*, 12(7):e1004988, July 2016.

[19] Jian-Geng Chiou, Mohan K Balasubramanian, and Daniel J Lew. Cell polarity in yeast. *Annu. Rev. Cell Dev. Biol.*, 33:77–101, October 2017.

[20] Neus Colomina, Francisco Ferrezuelo, Emili Vergés, Martí Aldea, and Eloi Garí. Whi3 regulates morphogenesis in budding yeast by enhancing cdk functions in apical growth. *Cell Cycle*, 8(12):1912–1920, 2009.

[21] Ira R Cooke, Kurt Kremer, and Markus Deserno. Tunable generic model for fluid bilayer membranes. *Physical Review E*, 72(1):011506, 2005.

[22] Etienne Dague, Rajaa Bitar, Hubert Ranchon, Fabien Durand, Hélène Martin Yken, and Jean M François. An atomic force microscopy analysis of yeast mutants defective in cell wall architecture. *Yeast*, 27(8):673–684, August 2010.

[23] Iñigo Martinez De, Pierre-André Marechal, and Patrick Gervais. Passive response ofsaccharomyces cerevisiaeto osmotic shifts: Cell volume variations depending on the physiological state. *Biochem. Biophys. Res. Commun.*, 227(2):519–523, October 1996.

[24] G I de Becze. A microbiological process report; yeasts. i. morphology. *Appl. Microbiol.*, 4(1):1–12, January 1956.

[25] Julien Delile, Matthieu Herrmann, Nadine Peyriéras, and René Doursat. A cell-based computational model of early embryogenesis coupling mechanical behaviour and gene regulation. *Nature communications*, 8(1):1–10, 2017.

[26] Hua Deng, Prashanta Dutta, and Jin Liu. Stochastic simulations of nanoparticle internalization through transferrin receptor dependent clathrin-mediated endocytosis. *Biochim. Biophys. Acta Gen. Subj.*, 1862(9):2104–2111, September 2018.

[27] D G Drubin. Development of cell polarity in budding yeast. *Cell*, 65(7):1093–1096, June 1991.

[28] Helge Ewers and Ari Helenius. Lipid-mediated endocytosis. *Cold Spring Harbor perspectives in biology*, 3(8):a004721, 2011.

[29] Reza Farhadifar, Jens-Christian Röper, Benoit Aigouy, Suzanne Eaton, and Frank Jülicher. The influence of cell mechanics, cell-cell interactions, and proliferation on epithelial packing. *Curr. Biol.*, 17(24):2095–2104, December 2007.

[30] Dmitry A Fedosov, Huan Lei, Bruce Caswell, Subra Suresh, and George E Karniadakis. Multiscale modeling of red blood cell mechanics and blood flow in malaria. *PLoS Comput. Biol.*, 7(12):e1002270, December 2011.

[31] Shuo Feng, Yucai Hu, and Haiyi Liang. Entropic elasticity based coarse-grained model of lipid membranes. *The Journal of chemical physics*, 148(16):164705, 2018.

[32] Francisco Ferrezuelo, Neus Colomina, Alida Palmisano, Eloi Garí, Carme Gallego, Attila Csikász-Nagy, and Martí Aldea. The critical size is set at a single-cell level by growth rate to attain homeostasis and adaptation. *Nature communications*, 3(1):1–11, 2012.

[33] Xinli Gao, Junjun Dong, and Xianren Zhang. The effect of nanoparticle size on endocytosis dynamics depends on membrane–nanoparticle interaction. *Molecular Simulation*, 41(7):531–537, 2015.

[34] Marco Geymonat and Marisa Segal. Intrinsic and extrinsic determinants linking spindle pole fate, spindle polarity, and asymmetric cell division in the budding yeast s. cerevisiae. *Results Probl. Cell Differ.*, 61:49–82, 2017.

[35] Amy S Gladfelter, Indrani Bose, Trevin R Zyla, Elaine S G Bardes, and Daniel J Lew. Septin ring assembly involves cycles of GTP loading and hydrolysis by cdc42p. *J. Cell Biol.*, 156(2):315–326, January 2002.

[36] Amy S Gladfelter, Lukasz Kozubowski, Trevin R Zyla, and Daniel J Lew. Interplay between septin organization, cell cycle and cell shape in yeast. *J. Cell Sci.*, 118(Pt 8):1617–1628, April 2005.

[37] Oliver Glomb and Thomas Gronemeyer. Septin organization and functions in budding yeast. *Front Cell Dev Biol*, 4:123, November 2016.

[38] Björn Goldenbogen, Wolfgang Giese, Marie Hemmen, Jannis Uhlendorf, Andreas Herrmann, and Edda Klipp. Dynamics of cell wall elasticity pattern shapes the cell during yeast mating morphogenesis. *Open Biol.*, 6(9), September 2016.

[39] Ronald Goldman. Area of planar polygons and volume of polyhedra. *Graphics Gems II*, 01 2004.

[40] G Gompper and D M Kroll. Random surface discretizations and the renormalization of the bending rigidity. *J. Phys. I*, 6(10):1305–1320, October 1996.

[41] G Gompper and D M Kroll. Membranes with fluctuating topology: Monte carlo simulations, 1998.

[42] Bruce L Goode, Julian A Eskin, and Beverly Wendland. Actin and endocytosis in budding yeast. *Genetics*, 199(2):315–358, 2015.

[43] D R M Graham, E Chertova, J M Hilburn, and others. Cholesterol depletion of human immunodeficiency virus type 1 and simian immunodeficiency virus with $\beta$-cyclodextrin inactivates and permeabilizes the virions .... *Journal of*, 2003.

[44] Marie-Pierre Gulli, Malika Jaquenoud, Yukiko Shimada, Guy Niederhäuser, Philippe Wiget, and Matthias Peter. Phosphorylation of the cdc42 exchange factor cdc24 by the pak-like kinase cla4 may regulate polarized growth in yeast. *Molecular cell*, 6(5):1155–1167, 2000.

[45] Allison E Hall and Mark D Rose. Cell fusion in yeast is negatively regulated by components of the cell wall integrity pathway. *Molecular biology of the cell*, 30(4):441–452, 2019.

[46] AT Hammond, FA Heberle, T Baumgart, D Holowka, B Baird, and GW Feigenson. Crosslinking a lipid raft component triggers liquid ordered-liquid disordered phase separation in model plasma membranes. *Proceedings of the National Academy of Sciences*, 102(18):6320–6325, 2005.

[47] R Hanschke and F Schauer. Improved ultrastructural preservation of yeast cells for scanning electron microscopy. *J. Microsc.*, 184(Pt 2):81–87, November 1996.

[48] Nan Hao. The analysis of feedback regulation in yeast signal transduction pathways. August 2006.

[49] Ivan Hapala, Peter Griač, Jozef Nosek, Hana Sychrová, and Lubomír Tomáška. Yeast membranes and cell wall: from basics to applications. *Curr. Genet.*, 59(4):167–169, November 2013.

[50] P Heun, T Laroche, M K Raghuraman, and S M Gasser. The positioning and dynamics of origins of replication in the budding yeast nucleus. *J. Cell Biol.*, 152(2):385–400, January 2001.

[51] Audrey S Howell, Meng Jin, Chi-Fang Wu, Trevin R Zyla, Timothy C Elston, and Daniel J Lew. Negative feedback enhances robustness in the yeast polarity establishment circuit. *Cell*, 149(2):322–333, 2012.

[52] Audrey S Howell and Daniel J Lew. Morphogenesis and the cell cycle. *Genetics*, 190(1):51–77, January 2012.

[53] Ramon Hurtado-Guerrero, Alexander W Schüttelkopf, Isabelle Mouyna, Adel F M Ibrahim, Sharon Shepherd, Thierry Fontaine, Jean-Paul Latgé, and Daan M F van Aalten. Molecular mechanisms of yeast cell wall glucan remodeling. *J. Biol. Chem.*, 284(13):8461–8469, March 2009.

[54] Matt Kaeberlein. Lessons on longevity from budding yeast. *Nature*, 464(7288):513–519, March 2010.

[55] Marko Kaksonen and Aurélien Roux. Mechanisms of clathrin-mediated endocytosis. *Nat. Rev. Mol. Cell Biol.*, 19(5):313–326, May 2018.

[56] Marko Kaksonen and Aurélien Roux. Mechanisms of clathrin-mediated endocytosis. *Nature Reviews Molecular Cell Biology*, 19(5):313, 2018.

[57] Sudesh Kalyanswamy. Euler characteristic, 2009.

[58] Frans M Klis, Andre Boorsma, and Piet W J De Groot. Cell wall construction in saccharomyces cerevisiae. *Yeast*, 23(3):185–202, February 2006.

[59] Frans M Klis, Chris G de Koster, and Stanley Brul. Cell wall-related bionumbers and bioestimates of saccharomyces cerevisiae and candida albicans. *Eukaryotic cell*, 13(1):2–9, 2014.

[60] T Kohyama, D M Kroll, and G Gompper. Budding of crystalline domains in fluid membranes. *Phys. Rev. E Stat. Nonlin. Soft Matter Phys.*, 68(6 Pt 1):061905, December 2003.

[61] Roman Kollár, Bruce B Reinhold, Eva Petráková, Herman J C Yeh, Gilbert Ashwell, Jana Drgonová, Johan C Kapteyn, Frans M Klis, and Enrico Cabib. Architecture of the yeast cell wall: $\beta(1\rightarrow6)$-GLUCAN INTERCONNECTS MANNOPROTEIN, $\beta(1\rightarrow3)$-GLUCAN, AND CHITIN. *J. Biol. Chem.*, 272(28):17762–17775, July 1997.

[62] Benjamin Kollmitzer, Peter Heftberger, Rudolf Podgornik, John F Nagle, and Georg Pabst. Bending rigidities and interdomain forces in membranes with coexisting lipid domains. *Biophysical journal*, 108(12):2833–2842, 2015.

[63] Wanda Kukulski, Martin Schorb, Marko Kaksonen, and John AG Briggs. Plasma membrane reshaping during endocytosis is revealed by time-resolved electron tomography. *Cell*, 150(3):508–520, 2012.

[64] Helen Lai, Jian-Geng Chiou, Anastasia Zhurikhina, Trevin R Zyla, Denis Tsygankov, and Daniel J Lew. Temporal regulation of morphogenetic events in saccharomyces cerevisiae. *Mol. Biol. Cell*, 29(17):2069–2083, August 2018.

[65] Guillaume Lesage and Howard Bussey. Cell wall assembly in saccharomyces cerevisiae. *Microbiol. Mol. Biol. Rev.*, 70(2):317–343, June 2006.

[66] R Li and A W Murray. Feedback control of mitosis in budding yeast. *Cell*, 66(3):519–531, August 1991.

[67] Siyu Li, Polly Roy, Alex Travesset, and Roya Zandi. Why large icosahedral viruses need scaffolding proteins. *Proc. Natl. Acad. Sci. U. S. A.*, 115(43):10971–10976, October 2018.

[68] Athanasios Litsios, Daphne H E W Huberts, Hanna M Terpstra, Paolo Guerra, Alexander Schmidt, Katarzyna Buczak, Alexandros Papagiannakis, Mattia Rovetta, Johan Hekelaar, Georg Hubmann, Marten Exterkate, Andreas Milias-Argeitis, and Matthias Heinemann. Differential scaling between G1 protein production and cell size dynamics promotes commitment to the cell division cycle in budding yeast. *Nat. Cell Biol.*, 21(11):1382–1392, November 2019.

[69] Ying Luo, Jianguo Wang, Bin Liu, Zhouli Wang, Yahong Yuan, and Tianli Yue. Effect of yeast cell morphology, cell wall physical structure and chemical composition on patulin adsorption. *PLoS One*, 10(8):e0136045, August 2015.

[70] Simeone Marino, Ian B Hogue, Christian J Ray, and Denise E Kirschner. A methodology for performing global uncertainty and sensitivity analysis in systems biology. *J. Theor. Biol.*, 254(1):178–196, September 2008.

[71] Siewert J Marrink, Valentina Corradi, Paulo CT Souza, Helgi I Ingoélfsson, D Peter Tieleman, and Mark SP Sansom. Computational modeling of realistic cell membranes. *Chemical reviews*, 119(9):6184–6226, 2019.

[72] Uwe F Mayer. Numerical solutions for the surface diffusion flow in three space dimensions. *Computational and Applied Mathematics*, 20(3):361–379, 2001.

[73] M D McKay, R J Beckman, and W J Conover. Comparison of three methods for selecting values of input variables in the analysis of output from a computer code, 1979.

[74] Michael A McMurray, Aurelie Bertin, Galo Garcia, 3rd, Lisa Lam, Eva Nogales, and Jeremy Thorner. Septin filament formation is essential in budding yeast. *Dev. Cell*, 20(4):540–549, April 2011.

[75] Ira Mellman and Yosef Yarden. Endocytosis and cancer. *Cold Spring Harbor perspectives in biology*, 5(12):a016949, 2013.

[76] James B Moseley and Bruce L Goode. The yeast actin cytoskeleton: from cellular function to biochemical mechanism. *Microbiol. Mol. Biol. Rev.*, 70(3):605–645, September 2006.

[77] Yaron Mosesson, Gordon B Mills, and Yosef Yarden. Derailed endocytosis: an emerging feature of cancer. *Nature Reviews Cancer*, 8(11):835–850, 2008.

[78] Surendra Nahar, Sartaj Sahni, and Eugene Shragowitz. Simulated annealing and combinatorial optimization. In *23rd ACM/IEEE Design Automation Conference*, pages 293–299. IEEE, 1986.

[79] Ali Nematbakhsh, Megan Levis, Nilay Kumar, Weitao Chen, Jeremiah J. Zartman, and Mark Alber. Epithelial organ shape is generated by patterned actomyosin contractility and maintained by the extracellular matrix. *PLOS Computational Biology*, 16(8):1–24, 08 2020.

[80] Ali Nematbakhsh, Wenzhao Sun, Pavel A Brodskiy, Aboutaleb Amiri, Cody Narciso, Zhiliang Xu, Jeremiah J Zartman, and Mark Alber. Multi-scale computational study of the mechanical regulation of cell mitotic rounding in epithelia. *PLoS computational biology*, 13(5):e1005533, 2017.

[81] Takeshi Noda, Hideki Ebihara, Yukiko Muramoto, Ken Fujii, Ayato Takada, Hiroshi Sagara, Jin Hyun Kim, Hiroshi Kida, Heinz Feldmann, and Yoshihiro Kawaoka. Assembly and budding of ebolavirus. *PLoS pathogens*, 2(9), 2006.

[82] Hiroshi Noguchi and Gerhard Gompper. Fluid vesicles with viscous membranes in shear flow. *Phys. Rev. Lett.*, 93(25):258102, December 2004.

[83] Hiroshi Noguchi and Gerhard Gompper. Dynamics of fluid vesicles in shear flow: effect of membrane viscosity and thermal fluctuations. *Phys. Rev. E Stat. Nonlin. Soft Matter Phys.*, 72(1 Pt 1):011901, July 2005.

[84] Younghoon Oh and Erfei Bi. Septin structure and function in yeast and beyond. *Trends Cell Biol.*, 21(3):141–148, March 2011.

[85] Satoru Okuda and Mototsugu Eiraku. Role of molecular turnover in dynamic deformation of a three-dimensional cellular membrane, 2017.

[86] Akira Ono and Eric O Freed. Plasma membrane rafts play a critical role in hiv-1 assembly and release. *Proceedings of the National Academy of Sciences*, 98(24):13925–13930, 2001.

[87] Sanaz Panahandeh, Siyu Li, Laurent Marichal, Rafael Leite Rubim, Guillaume Tresset, and Roya Zandi. How a virus circumvents energy barriers to form symmetric shells. *ACS Nano*, 14(3):3170–3180, March 2020.

[88] Sanaz Panahandeh, Siyu Li, and Roya Zandi. The equilibrium structure of self-assembled protein nano-cages. *Nanoscale*, 10(48):22802–22809, December 2018.

[89] Hay-Oak Park and Erfei Bi. Central roles of small GTPases in the development of cell polarity in yeast and beyond. *Microbiol. Mol. Biol. Rev.*, 71(1):48–96, March 2007.

[90] C David Pauza and Todd M Price. Human immunodeficiency virus infection of t cells and monocytes proceeds via receptor-mediated endocytosis. *The Journal of cell biology*, 107(3):959–968, 1988.

[91] Heather A Pillman and GJ Blanchard. Consequences of transient heating on the motional dynamics of cholesterol-containing phospholipid vesicles. *The Journal of Physical Chemistry B*, 115(14):3819–3827, 2011.

[92] Stephen A Proctor, Nicolas Minc, Arezki Boudaoud, and Fred Chang. Contributions of turgor pressure, the contractile ring, and septum assembly to forces in cytokinesis in fission yeast. *Curr. Biol.*, 22(17):1601–1608, September 2012.

[93] Zhong Ming Qian, Hongyan Li, Hongzhe Sun, and Kwokping Ho. Targeted drug delivery via the transferrin receptor-mediated endocytosis pathway. *Pharmacological reviews*, 54(4):561–587, 2002.

[94] Michael Raatz, Reinhard Lipowsky, and Thomas R Weikl. Cooperative wrapping of nanoparticles by membrane tubes. *Soft Matter*, 10(20):3570–3577, May 2014.

[95] Teresa Ruiz-Herrero, Enrique Velasco, and Michael F Hagan. Mechanisms of budding of nanoscale particles through lipid bilayers. *J. Phys. Chem. B*, 116(32):9595–9603, August 2012.

[96] Mohsen Sadeghi, Thomas R Weikl, and Frank Noé. Particle-based membrane model for mesoscopic simulation of cellular dynamics. *The Journal of Chemical Physics*, 148(4):044901, 2018.

[97] Jörg Schaber, Miquel Angel Adrover, Emma Eriksson, Serge Pelet, Elzbieta Petelenz-Kurdziel, Dagmara Klein, Francesc Posas, Mattias Goksör, Mathias Peter, Stefan Hohmann, and Edda Klipp. Biophysical properties of saccharomyces cerevisiae and their relationship with HOG pathway activation. *Eur. Biophys. J.*, 39(11):1547–1556, October 2010.

[98] Martin Schmidt, Archana Varma, Tomás Drgon, Blair Bowers, and Enrico Cabib. Septins, under cla4p regulation, and the chitin ring are required for neck integrity in budding yeast. *Mol. Biol. Cell*, 14(5):2128–2141, May 2003.

[99] Prabuddha Sengupta, Barbara Baird, and David Holowka. Lipid rafts, fluid/fluid phase separation, and their relevance to plasma membrane structure and function. In *Seminars in cell & developmental biology*, volume 18, pages 583–590. Elsevier, 2007.

[100] Maya Shamir, Yinon Bar-On, Rob Phillips, and Ron Milo. Snapshot: timescales in cell biology. *Cell*, 164(6):1302–1302, 2016.

[101] Fred Sherman. Getting started with yeast. In Christine Guthrie and Gerald R Fink, editors, *Methods in Enzymology*, volume 350, pages 3–41. Academic Press, January 2002.

[102] Yi-Jun Sheu, Yves Barral, and Michael Snyder. Polarized growth controls cell shape and bipolar bud site selection in saccharomyces cerevisiae. *Molecular and cellular biology*, 20(14):5235–5247, 2000.

[103] A E Smith, Z Zhang, and C R Thomas. Wall material properties of yeast cells: Part 1. cell measurements and compression experiments. *Chem. Eng. Sci.*, 55(11):2031–2041, June 2000.

[104] Jean A Smith, Allison E Hall, and Mark D Rose. Membrane curvature directs the localization of cdc42p to novel foci required for cell–cell fusion. *Journal of Cell Biology*, 216(12):3971–3980, 2017.

[105] Eric J Spangler, Sudhir Upreti, and Mohamed Laradji. Partial wrapping and spontaneous endocytosis of spherical nanoparticles by tensionless lipid membranes. *The Journal of chemical physics*, 144(4):044901, 2016.

[106] Mingzhai Sun, Nathan Northup, Francoise Marga, Tamas Huber, Fitzroy J Byfield, Irena Levitan, and Gabor Forgacs. The effect of cellular cholesterol on membrane-cytoskeleton adhesion. *J. Cell Sci.*, 120(Pt 13):2223–2231, July 2007.

[107] Wesley I Sundquist and Hans-Georg Kräusslich. Hiv-1 assembly, budding, and maturation. *Cold Spring Harbor perspectives in medicine*, 2(7):a006924, 2012.

[108] Michael Trogdon, Brian Drawert, Carlos Gomez, Samhita P Banavar, Tau-Mu Yi, Otger Campàs, and Linda R Petzold. The effect of cell geometry on polarization in budding yeast. *PLoS Comput. Biol.*, 14(6):e1006241, June 2018.

[109] Kevin Tsai, Samuel Britton, Ali Nematbakhsh, Roya Zandi, Weitao Chen, and Mark Alber. Role of combined cell membrane and wall mechanical properties regulated by polarity signals in cell budding. *Physical Biology*, 2020.

[110] Roman Vetter, Norbert Stoop, Falk K Wittel, and Hans J Herrmann. Simulating thin sheets: Buckling, wrinkling, folding and growth - IOPscience. `https://iopscience.iop.org/article/10.1088/1742-6596/487/1/012012`. Accessed: 2020-4-20.

[111] Jef Wagner and Roya Zandi. The robust assembly of small symmetric nanoshells. *Biophys. J.*, 109(5):956–965, September 2015.

[112] Shigeki Watanabe and Emmanuel Boucrot. Fast and ultrafast endocytosis. *Current opinion in cell biology*, 47:64–71, 2017.

[113] Roland Wedlich-Soldner, Steve Altschuler, Lani Wu, and Rong Li. Spontaneous cell polarization through actomyosin-based delivery of the cdc42 GTPase. *Science*, 299(5610):1231–1235, February 2003.

[114] Hyeong-Cheol Yang and Liza A Pon. Actin cable dynamics in budding yeast. *Proc. Natl. Acad. Sci. U. S. A.*, 99(2):751–756, January 2002.

[115] Xin Yi, Xinghua Shi, and Huajian Gao. Cellular uptake of elastic nanoparticles. *Physical review letters*, 107(9):098101, 2011.

[116] X Zhang, E Bi, P Novick, L Du, K G Kozminski, J H Lipschutz, and W Guo. Cdc42 interacts with the exocyst and regulates polarized secretion. *J. Biol. Chem.*, 276(50):46745–46750, December 2001.